CHAPTER ONE

Multiscale geometry and mechanics of lipid monolayer collapse

Angelo Rosario Carotenuto^{a,b}, Nhung Nguyen^b, Kathleen Cao^b, Anna Gaffney^c, Alan J. Waring^d, Ka Yee C. Lee^e, David Owen^f, Massimiliano Fraldi^a, Luca Deseri^{g,h,i,j,*}, and Luka Pocivavsek^{b,*}

Contents

1.	Introduction	2
2.	Methods	6
	2.1 Experimental procedure	6
	2.2 Finite element modeling	9
3.	Experimental results	13
	3.1 Image analysis	14
	3.2 Isotherm analysis	19
4.	Finite element analysis	23
5.	Multiscale geometry of lipid monolayers	29
	5.1 A closer look at conformational changes	33
	5.2 Macroscopic deformation	37
	5.3 A measure of geometrical changes without disarrangements	38
	5.4 Positional disarrangements	40
6.	Conclusions	40
Acknowledgments		41
References		41

^aDepartment of Structures for Engineering and Architecture, University of Napoli "Federico II", Naples, Italy

^bDepartment of Surgery, The University of Chicago, Chicago, IL, United States

^cProgram in Biophysical Sciences, The University of Chicago, Chicago, IL, United States

^dDepartment of Medicine, UCLA School of Medicine, Los Angeles, CA, United States

^eDepartment of Chemistry, The University of Chicago, Chicago, IL, United States ^fDepartment of Mathematical Sciences, Carnegie Mellon University, Pittsburgh, PA, United States

Bepartment of Civil, Environmental and Mechanical Engineering, University of Trento, Trento, Italy

^hDepartment of Mechanical Engineering and Material Sciences, SSoE, University of Pittsburgh, PA, United States

ⁱDepartment of Civil and Environmental Engineering, Department of Mechanical Engineering, Carnegie Mellon University, Pittsburgh, PA, United States

^jDepartment of Nanomedicine, The Houston Methodist Research Institute, Houston, TX, United States *Corresponding authors: e-mail address: luca.deseri@unitn.it; lpocivavsek@bsd.uchicago.edu

Abstract

Langmuir monolayers at gas/liquid interfaces provide a rich framework to investigate the interplay between multiscale geometry and mechanics. Monolayer collapse is investigated at a topological and geometric level by building a scale space ${\mathcal M}$ from experimental imaging data. We present a general lipid monolayer collapse phase diagram, which shows that wrinkling, folding, crumpling, shear banding, and vesiculation are a continuous set of mechanical states that can be approached by either tuning monolayer composition or temperature. The origin of the different mechanical states can be understood by investigating the monolayer geometry at two scales: fluorescent vs atomic force microscopy imaging. We show that an interesting switch in continuity occurs in passing between the two scales, $\mathcal{C}_{AFM} \in \mathcal{M}_{AFM} \neq \mathcal{C}_{FM} \in \mathcal{M}$. Studying the difference between monolayers that fold vs shear band, we show that shear banding is correlated to the persistence of a multi-length scale microstructure within the monolayer at all surface pressures. A detailed analytical geometric formalism to describe this microstructure is developed using the theory of structured deformations. Lastly, we provide the first ever finite element simulation of lipid monolayer collapse utilizing a direct mapping from the experimental image space \mathcal{M} into a simulation domain \mathcal{P} . We show that elastic dissipation in the form of bielasticity is a necessary and sufficient condition to capture loss of in-plane stability and shear banding.

1. Introduction

For nearly a century, Langmuir monolayers have provided a rich system for the study of self-organizing matter. The importance of surfactants in industrial applications is hard to underestimate (Safran, 1994). Furthermore, lipids are among the essential building blocks of living matter, their organization into bilayers forms cell membranes (Boal, 2002; Fung, 1993). Lipid membranes play an integral role in creating multicellular tissues whose organization ultimately leads to organisms (Boal, 2002). Moreover, the lipid membrane is critical in intracellular interactions and specifically in helping transmit mechanical information from one cell to another (Junghans et al., 2014, 2015; Pocivavsek, Junghans, Zebda, Birukov, & Majewski, 2013). Lipid monolayers also play important biological roles, especially in animals with lungs, where the surfactant monolayer reduces surface tension of the large air/water interface needed for gas exchange (Piknova, Schram, & Hall, 2002; Robertson & Halliday, 1998; Zasadzinski, Ding, Warriner, Bringezu, & Waring, 2001). The lipid monolayer's or bilayer's response to mechanical forces is integral to many roles lipids play in biological systems (Gopal & Lee, 2001; Lipp, Lee, Takamoto, Zasadzinski, & Waring, 1998; Ybert, Lu, Möller, & Knobler, 2002 a, 2002 b). However, we lack a general understanding of lipid mechanics under many biologically relevant conditions.

Historically the approach to lipid mechanics began with thermodynamics, especially in monolayers. The Langmuir monolayer's confinement to the two-dimensional gas/liquid interface allows direct visualization of thermodynamics at work. The study of in-plane lipid phase transitions is among the most studied monolayer phenomena (Kaganer, Möhwald, & Dutta, 1999; McConnell, 1991; Möhwald, 1990, 1993). Various phases have been identified throughout the decades (see Fig. 1), including gaseous, liquid expanded (LE), liquid condensed (LC), solid, and many subtypes (Möhwald, 1990, 1993; Safran, 1994). Pioneering monolayer work was later extended

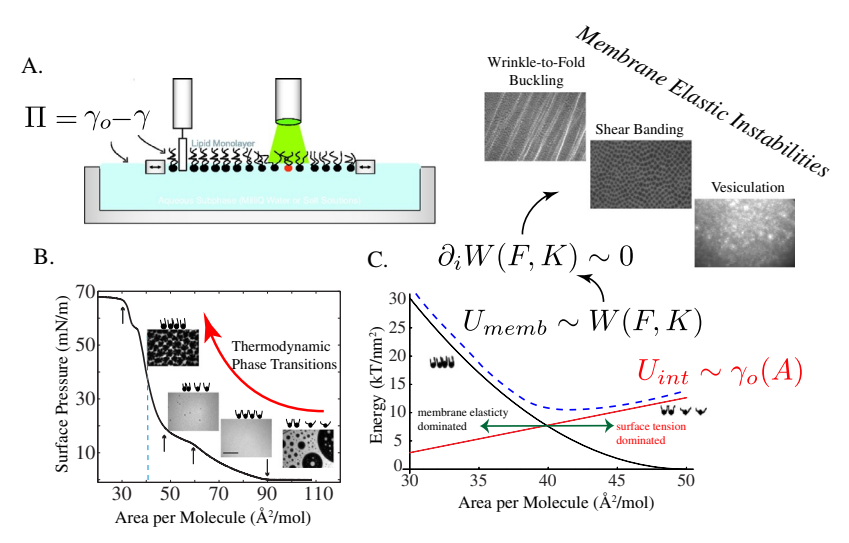


Fig. 1 All lipid monolayers in this paper were prepared as Langmuir monolayers spread at a gas/water interface. The details of the setup are provided in the methods. Panel (A) shows a schematic of the Langmuir trough with two barriers used to control the lipid density at the interface. A Wilhelmy surface balance is used to measure the lateral surface pressure, which is given as the difference in surface tensions of a lipid free and lipid covered interface, $\Pi = \gamma_o - \gamma$. It should be noted that in general $\Pi/h \neq \sigma_{ii}$, where h is monolayer thickness and σ_{ii} is the true stress in the monolayer; furthermore only when the monolayer is a liquid, unable to sustain a static shear stress, does Π represent the hydrostatic pressure (Witten et al., 2010). Panel (B) shows a representative isotherm with the three canonical thermodynamic lipid phases: gas, liquid expanded (LE), and liquid condensed (LC). Panel (C) shows lipid monolayer energy as a function of inverse density (area per lipid molecule). At low packing density (gas and LE phases), the monolayer energy is dominated by the interfacial energy which is well represented by $U \sim \Pi$. h/A. However, as the monolayer transitions into an elastic solid, beginning with the LC phase, a membrane elastic energy term emerges, $U_{memb} \sim W(F, K)$, where F is the macroscopic deformation gradient and K the component due to positional disarrangements according to the theory of structured deformations. Minimization of W(F, K) provides a general framework in which to study the wide range of elastic instabilities seen in solid-like lipid monolayers.

to bilayers under various configurations: supported bilayers, vesicles, etc. (Kaganer et al., 1999; McConnell, 1991; Möhwald, 1990, 1993). Quantitative modeling of lipid thermodynamics is largely rooted in the development of equations of state and their validation with experiments, such as isotherm measurements using a Langmuir trough (see Fig. 1) (Andelman, Brochard, Knobler, & Rondelez, 1994; Fennell Evans & Wennerström, 1999; Kaganer et al., 1999; McConnell, 1991; Pocivavsek, Frey, et al., 2008; Pocivavsek et al., 2011).

Langmuir monolayers have also proven to be ideal systems to study lipid mechanics in highly confined geometries or high lipid packing densities, where the system is believed to behave as an elastic continuum. Ries (1979) first observed a solid-like response in monolayers where trilayered structures appeared on top of the monolayer at high compression; he hypothesized a simple mechanical model based on elastic plate buckling to explain the observed multilayers (Ries, 1979). Other experimental work confirmed the peculiar folding behavior of a variety of lipid and gold nanoparticle films (Gopal & Lee, 2001; Lin et al., 2007; Lipp et al., 1998; Schultz et al., 2006; Ybert et al., 2002 a, 2002 b). It would be more than 50 years until a quantitative model of monolayer folding was developed by Pocivavsek, Dellsy, et al. (2008). The wrinkle-to-fold model treated the lipid monolayer as a uniform elastic plate which under compression buckles with a given wavelength; with further compression, the linearly stable wrinkles convert to localized nonlinear folds which can lead to the multilayer structures observed experimentally (Pocivavsek, Dellsy, et al., 2008). Treating the monolayer as a homogeneous elastic plate essentially extracted only the most basic geometric structure of the monolayer to build a mechanical model. Yet this highly reduced approach was able to quantitatively predict collapse features to a much larger extent than models which approached collapse (loss of mechanical stability) from the standpoint of thermodynamic defects (Diamant, Witten, Ege, Gopal, & Lee, 2001; Diamant, Witten, Gopal, & Lee, 2000; Lu, Knobler, Bruinsma, Twardos, & Dennin, 2002; Nikomarov, 1990; Saint-Jalmes, Assenheimer, & Gallet, 1998; Saint-Jalmes, Graner, Gallet, & Houchmandzadeh, 1994; Saint-Jalmes & Gallet, 1998).

More recent research in monolayer collapse mechanisms has examined a broad range of topics. In lipid monolayers, the exploration of membrane composition has found net charge, acyl chain saturation, and presence of cholesterol to have important roles in altering collapse structures through tuning in-plane rigidity (Garg, Thomas, & Borden, 2013; Goto & Caseli, 2013;

Kim, Choi, Zell, Squires, & Zasadzinski, 2013; Thomas & Borden, 2017; Zhang, Fan, Wang, Neal, & Zuo, 2011). These findings reveal insights into the mechanical properties and collapse of various clinical surfactants. Presence of polymers (Callens et al., 2019) and surfactant proteins (Holten-Andersen et al., 2011; Pocivavsek, Frey, et al., 2008) in the composition of lipid monolayers has been found to act as mechanical instabilities which lead to folding and collapse. Introduction of small molecules such as glycerol to the subphase can amplify the size of the folds upon monolayer collapse due to their enrichment at the lipid headgroup interface (Pocivavsek et al., 2011). While much of this work has been conducted using Langmuir trough experiments, lipidcoated microbubbles have emerged as innovative tools to study monolayer collapse and stabilization, with additional biological and medical implications (Garg et al., 2013; Kwan & Borden, 2012a, 2012b; Thomas & Borden, 2017). Monolayers composed of various nanoparticles offer a range of exploration into nonlinear surface pressure near buckling (Cicuta & Vella, 2009; Liu, Sun, & Santamarina, 2021) and the critical role of in-plane rigidity for out-of-plane wrinkling (Silverberg & Vecitis, 2017), due to the granular nature of the interface. Gold nanoparticle monolayers in particular show interesting features when forming localized regions of instability, which collapse upon compression into trilayers that can bend and fold depending on in-plane and out-of-plane mechanical properties (Chua et al., 2013; Leahy et al., 2010). In addition to the topology of monolayer collapse, the kinetics of such folding has been explored for some lipids (Boatwright, Levine, & Dennin, 2010; Kim et al., 2013; Oppenheimer, Diamant, & Witten, 2013) where in-plane rigidity is important in modeling and predicting the behavior.

We present a combined experimental, computational, and geometric analysis of lipid monolayer collapse. As noted above, a large amount of lipid literature focuses on the differences, often compositional, between different lipid systems. However, mechanical response, including collapse, is by its very nature a continuum phenomenon, as such it seeks commonalities. We set the ground work here for a general theory of lipid monolayer mechanics. We expand upon the linearly elastic plate models used to successfully describe monolayer folding (Pocivavsek, Dellsy, et al., 2008). The paper is divided into three parts. First, we present a novel general lipid monolayer collapse phase diagram, showing that five canonical modes of collapse can be accessed across lipid compositions and temperatures. We provide a scale space analysis of monolayer imaging data at multiple length scales, which builds a topology for the available monolayer data. Second, we present the first ever finite element simulation of lipid monolayers using

experimentally derived input geometries. The simulations allow us to systematically test how mechanical dissipation in portions of the monolayer leads to monolayer rearrangements and collapse via banding. Third, we utilize the rich theoretical machinery of structured deformations to set up the multiscale geometry of lipid monolayers based upon our experimental data.



2. Methods

2.1 Experimental procedure

2.1.1 Lipids, peptides, subphase, superphase

DMPE (1,2-dimyristoyl-sn-glycero-3-phosphoethanolamine, $T_m = 50$ °C), DPPC (1,2-dipalmitoyl-sn-glycero-3-phosphocholine, $T_m = 41^{\circ}$ C), POPG (1-palmitoyl-2-oleoyl-sn-glycero-3-phospho-(1-rac-glycerol)(sodium $T_m = -2$ °C), and GM1 (ovine brain ganglioside GM1) were obtained from Avanti Polar Lipids, Inc. (Alabaster, AL) in powder form and used without further purification. Lipids were either dissolved in chloroform (DPPC and POPG) or 9/1 (v/v) chloroform/methanol (DMPE and GM1) to make 5 mg/mL stock solutions. Solvents were HPLC grade and obtained from Fisher Scientific (Pittsburgh, PA). SP-B 9-25 is a truncated synthetic peptide of the 79-residue lung surfactant protein B. The peptide is an amphipathic helix with an amino acid sequence of WLCRALIKRIQAMIPKG. SP-B 9-25 was prepared using Fmoc chemistry (Fields, Lloyd, Macdonald, Otteson, & Noble, 1991; Waring et al., 2005) (double coupling, 2×45 min) with reagents from Applied Biosystems (Foster City, CA) with a 431A solid phase peptide synthesizer (Applied Biosystems, Foster City, CA) or a Symphony/Multiplex SPPS synthesizer (Protein Technologies, Tucson, AZ). The peptide was cleaved using modified Reagent K (90% trifluoroacetic acid, 4.4% triisopropyl silane, 2.2% thioanisol, and 4.4% water). The peptide was precipitated upon the addition of ice-cold diethyl ether, collected by centrifugation, and purified by reversed-phase HPLC. MALDI-TOF mass spectrometry using an ABI Voyager RP-RBT2 reflection time-of-flight mass spectrometer (Applied Biosystems, Foster City, CA) confirmed the predicted molecular mass of the peptide.

Lipid and lipid:peptide mixtures were prepared in several molar ratios: pure DMPE, DPPC:POPG 7:3, DPPC:POPG:SP-B 9-25 70:30:2, DPPC: GM1 8:2, and DPPC:GM1 5:5. The solutions were diluted with chloroform to obtain spreading solutions of concentration 0.1 mg/mL. Visualization with fluorescence microscopy was possible upon addition of 0.5 mol% Texas Red 1,2-dihexadecanoyl-sn-glycerol-3-phosphoethanolamine,

triethylammonium salt (TR-DHPE) (Invitrogen, Carlsbad, CA) to the spreading solutions. The subphase for all the experiments was ultrapure water (resistivity \geq 18 M Ω cm) made using a ultrapurification (Milli-Q Advantage A10, Millipore, Bedford, MA). The superphase was air except for experiments with monolayers containing POPG. To minimize oxidative damage to the unsaturated oleoyl chain of POPG, ultrahigh purity Argon 5.0 (Airgas, Chicago, IL) was used as the superphase.

2.1.2 Instrument setup

All monolayer experiments were performed using a home-built Langmuir trough system (Gopal & Lee, 2001). The set-up consists of a Teflon trough $(27.5 \times 6.35 \times 0.63 \text{ cm})$ fitted with two symmetrically mobile Teflon barriers (l = 6.35 cm). The barriers were placed on linear translational stages (UTM100CC, Corp., Irvine, CA) and interfaced to a Newport MM2000 motion controller to obtain movements with micron precision. The entire Langmuir trough also sits on x, y, and z translation stages (Newport Corp., Irvine, CA) that allow for scanning of the air/water interface in each of those respective directions. The surface pressure measurements are made using a Wilhelmy plate tensiometer (Riegler & Kirstein GmbH, Potsdam, Germany). As the surface area is reduced (compression) or increased (expansion), the change in surface pressure is monitored, giving rise to surface pressure (Π) vs area (A) isotherms. Temperature of the water subphase is maintained within 0.5°C of the target temperature using a home-built control assembly consisting of thermoelectric units (Omega Engineering Inc., Stamford, CT) attached to a heat sink maintained at 20°C by a Neslab RTE-100 water circulator (Portsmouth, NH). The trough is kept covered with a resistively heated indium-tin oxide- coated glass plate (Delta Technologies, Dallas, TX), which is maintained at approximately 2°C above the target subphase temperature in order to minimize air currents, reduce evaporative losses, and prevent condensation of water on the microscope objective. Direct imaging of the surface is performed using a fluorescence microscope with either a 50X or 20X extra-long working distance objective lens (Nikon Y-FL, Fryer Co., Huntley, IL). The filter cube (Nikon HYQ Texas Red, Fryer Co., Huntley, IL) used permits excitation between 530 and 590 nm and emission between between 610 and 690 nm. A CCD camera Photonics, Inc., Palo Alto, CA) is used to collect images at 30 frames/s, which are recorded on a Sony miniDV digital video cassette recorder (B&H Photo-Video, New York, NY). The space between the trough and microscope objective was confined in a Sigma Atmos glove-bag (Sigma-Aldrich, St. Louis, MO) to reduce air currents or to

achieve the argon superphase when necessary. The entire trough/microscope assembly is mounted on a vibration isolation table (Newport Corp., Irvine, CA) and controlled completely by a custom software interface written using LabView 6.1 (National Instruments, Dallas, TX).

2.1.3 Isothermal compression measurements

For each monolayer experiment, 80 mL of water was poured into the trough. The subphase was heated to 25, 32, or 37°C in the case of DPPC:POPG, 25°C for DPPC:POPG:SP-B 9-25, 30°C for DPPC: GM1, and 15, 25, or 37°C for DMPE. When the target temperature was reached, the surface balance was calibrated to the value of surface tension of pure water for that temperature (Vargaftik, Volkov, & Voljak, 1983). The monolayer was then spread at the gas/water interface by gently depositing drops onto the surface and allowed to equilibrate for 20 min. The barrier compression was started (linear speed of 0.1 mm/s) and isotherm data as Π (mN/m) vs A (\mathring{A}^2 /molecule) were collected at 1-s intervals. The surface was imaged continuously throughout the compression.

2.1.4 Atomic force microscopy measurements

In order to study the surface morphology with nanometer resolution, the monolayer at a given surface pressure was deposited onto a freshly cleaved high grade mica surface (Ted Pella, Inc., Redding, CA) using an inverse Langmuir-Schaefer technique (Lee et al., 1998) and subsequently imaged by atomic force microscopy (AFM). The AFM mica puck was placed in a custom-machined stainless steel washer with a knife sharp rim (2 mm above the mica surface) and placed at the bottom of the trough prior to the addition of the subphase. The monolayer was isothermally compressed to the desired surface pressure. The subphase was slowly removed by suction, lowering the monolayer until it was cut by the washer knife edge. Three holes drilled into the bottom of the washer allowed the subphase to drain from the chamber until the monolayer was completely deposited onto the mica substrate. This method allowed us to keep the monolayer morphology and density intact throughout the deposition process. The mica supported monolayers were imaged in air with a Multimode Nanoscope IIIA scanning probe microscope (Digital Instruments, Santa Barbara, CA) with a Type J scanner in contact mode using silicon nitride tips (NP-S, Veeco Probes, Woodbury, NY) with a nominal spring constant of 0.32 N/m. The tips were decontaminated by ultraviolet generated ozone (PSD-UV Surface Decontamination System, Novascan, Ames, IA) prior to their use.

2.2 Finite element modeling

Since banding in lipid monolayers as observed in the above experimental data occurs when the monolayers are in a solid rather than liquid state, continuum mechanics and finite element (FE) method are promising tools to provide significant insight into its underlying mechanism. Thus, we integrate principles of nonlinear, large deformation solid mechanics with finite element analysis (FEA) to investigate this complex system. FE simulations are implemented using the commercial software package Abaqus 2018 (Dassault Systèmes Americas Corp., Waltham, MA) with the dynamic explicit solver. In order to construct an FE model for the lipid monolayer, the fluorescence image of the monolayer before banding is imported into the Simpleware ScanIP software (Synopsys, Inc., Mountain View, CA) to segment out the solid and continuous phases. After this segmentation, the lipid model can be meshed either in ScanIP or in Abaqus (note that in general, we found the meshing algorithm in ScanIP to be more flexible and provided better mesh quality than Abaqus). A representative FE model for a lipid monolayer considered in this study is shown in Fig. 6. Here a square portion of the monolayer is extracted from the tested lipid monolayer and ScanIP allows the determination of both solid and continuous phases as well as their boundaries. The part with two distinguished phases is then imported into Abaqus and kinematic coupling constraints are then used to tie the common interface between the two phases.

Here, three-dimensional elements (C3D8R, 8-node linear brick, reduced integration, with hourglass control) were used to mesh both phases of the monolayer and a very fine mesh is employed. With a focus on the in-plane banding of the monolayer, and to reduce the complexity of the simulations as well as the computational time, an effective plane strain boundary condition in the out-of-plane direction (z) is used here. The monolayer is then subjected to equal compression from both left and right sides to represent the loading condition in the experimental setup described above.

A hyperelastic material behavior based on neo-Hookean strain energy function is used to model the elastic deformations of the solid domain, \mathcal{D} -phase, and the continuous \mathcal{C}_{FM} -phase of the monolayer as follows (Dassault Systèmes, 2018; Nguyen & Waas, 2016):

$$W_d = \frac{\mu_d}{2} (\bar{I}_1 - 3) + \frac{1}{D_d} (J - 1)^2 \tag{1}$$

$$W_{c} = \frac{\mu_{c}}{2} (\bar{I}_{1} - 3) + \frac{1}{D_{c}} (J - 1)^{2}$$
 (2)

where d and c subscripts indicate the domain and the continuous phase, respectively. μ is the shear modulus, K is the bulk modulus, and $D = \frac{2}{K}$ is used to numerically impose a quasi-incompressibility condition. Note that Abaqus explicit cannot model fully incompressibile materials but requires a certain level of compressibility. As K/μ gets large, the model approaches the incompressibility condition, where the volume change J = det(F) equals to 1. Here, F is the deformation gradient and I_1 is the first invariant of the right Cauchy-Green tensor $C = F^T F$, and $\bar{I}_1 = J^{-2/3} I_1$ is the deviatoric part of the first invariant.

The strain energy function is used to derive the stress–strain relationship for a neo-Hookean behavior of the following form (Dassault Systèmes, 2018; Nguyen & Waas, 2016):

$$S = 2\frac{\partial W}{\partial C} \tag{3}$$

$$\sigma = \frac{1}{J}FSF^{T} \tag{4}$$

where S and σ are the second Piola–Kirchhoff and the Cauchy stresses, respectively. $W=W_d$, $S=S_d$, $\sigma=\sigma_d$ and $W=W_c$, $S=S_c$, $\sigma=\sigma_c$ for the \mathcal{D} and the \mathcal{C}_{FM} -phase, respectively. Thus, the Cauchy stress, becomes:

$$\sigma_d = \frac{1}{I} \mu_d \left\{ \bar{B} - \frac{1}{3} \bar{I}_1 I \right\} + \frac{2}{D_d} (J - 1) \tag{5}$$

$$\sigma_{\epsilon} = \frac{1}{I} \mu_{\epsilon} \left\{ \bar{B} - \frac{1}{3} \bar{I}_{1} I \right\} + \frac{2}{D_{\epsilon}} (J - 1) \tag{6}$$

where $B = FF^T$ is the left Cauchy Green tensor and $\bar{B} = J^{-2/3}B$.

While the domain acts like a homogeneous, rigid inclusion during the compression process, the continuous matrix is less rigid with a heterogeneous microstructure (see Fig. 4). Hence, the neo-Hookean strain energy function with fixed shear (μ_d) and bulk (K_d) moduli is assumed for the domain through the whole compression process. The stress is evolved during the compression process according to Eq. (5). On the other hand, the presence of the microstructures in the continuous phase might provide mechanisms for changes in its material properties and possibility for energy dissipation. We assume that such changes can be associated with the nucleation of banding observed in the monolayer. Here, we test such an assumption that the microstructures rearrange and lead to a material softening in

the continuous phase which may help to facilitate the banding instability phenomenon in the monolayer. For this purpose, in addition to the pure neo-Hookean model with the fixed shear (μ_c) and bulk (K_c) moduli where the stress is evolved according to Eqs. (2) and (6), three additional constitutive models that allow the considerations of softening and/or energy dissipation for the continuous phase are considered.

For the first two models, we assume that the continuous phase can be softened, or equivalently, there is a switch in the stress-deformation relationship that leads to a slower increase of the stress under an increase of deformation, when the von Mises stress reaches a critical value ($\sigma_{vm} = \sigma_{critical}$). To model the switch of the material behavior after this critical point, the first approach is to use the built-in elastic-plastic model in Abaqus where the critical stress is the yield stress σ_{vl} . Prior to this critical stress, the monolayer behaves elastically as a neo-Hookean solid with the shear (μ_c) and bulk (K_c) moduli described by the strain energy function in Eqs. (2) and (6). When the critical stress is reached, $\sigma_{vm} = \sigma_{critical}$, plasticity is activated that allows plastic flow and energy dissipation in the material model. As yielding occurs, the evolution of the stress is described as a function of the plastic strain. Due to the presence of the plastic strain, the stress no longer depends on the strain elastically as governed by the neo-Hookean strain energy in Eqs. (2) and (6), instead it increases in a slower fashion as the deformation increases. Though lipid monolayers are not likely to behave plastically, this numerical model allows the study of the effect of material instability on the shearing mechanism in the monolayer. The second approach is motivated by the consideration of the material softening due to microstructure rearrangement through prescribing a reduction of the shear modulus but without considering the plasticity effect as in the Abaqus built-in elastic-plastic model which can be nonphysical for lipid monolayers. Specifically, the shear modulus of the C-phase μ_c is reduced when the von Mises stress reaches a critical value. The strain energy in Eq. (2) is modified in a piecewise fashion with $\mu_c = \mu_{c1}$ for $\sigma_{vm} < \sigma_{critical}$ and $\mu_c = \mu_{c2} < \mu_{c1}$ for $\sigma_{vm} \ge \sigma_{critical}$, which is the shear modulus of the continuous matrix before material instability.

$$W_{c} = \frac{\mu_{c1}}{2} (\bar{I}_{1} - 3) + \frac{1}{D_{c1}} (J - 1)^{2} \quad \text{for} \quad \sigma_{vm} < \sigma_{critical}$$
 (7)

$$W_c = \frac{\mu_{c2}}{2} (\bar{I}_1 - 3) + \frac{1}{D_{c2}} (J - 1)^2 \quad \text{for} \quad \sigma_{vm} \ge \sigma_{critical}$$
 (8)

Through adjusting the ratio $\mu_{c1}/\mu_{c_2} \ge 1$, different levels of softening effects are examined. Note that when $\mu_{c1}/\mu_{c_2} = 1$, the C-phase becomes a pure

neo-Hookean material. This second approach (referred here as a "bielastic" model) is implemented in Abaqus explicit through the user material subroutine VUMAT (Dassault Systèmes, 2018). This subroutine is written in Fortran and requires the update of the current Cauchy stress in the material. The Cauchy stresses are derived from the neo-Hookean energies stated in Eqs. (7) and (8) and are updated as follows:

$$\sigma_{c} = \frac{1}{J} \mu_{c1} \left\{ \bar{B} - \frac{1}{3} \bar{I}_{1} I \right\} + \frac{2}{D_{c1}} (J - 1) \quad \text{for} \quad \sigma_{vm} < \sigma_{critical}$$
 (9)

$$\sigma_{c} = \frac{1}{J} \mu_{c2} \left\{ \bar{B} - \frac{1}{3} \bar{I}_{1} I \right\} + \frac{2}{D_{c2}} (J - 1) \quad \text{for} \quad \sigma_{vm} \ge \sigma_{critical} \tag{10}$$

For VUMAT subroutine's implementation, since the corotational coordinate system is used in Abaqus, only the stretch part is employed in updating the Cauchy stress. Hence, in the VUMAT subroutine, the Cauchy stress is calculated as follows:

$$\sigma_{c} = \frac{1}{J} \mu_{c} \left\{ \bar{U} - \frac{1}{3} \bar{I}_{1} I \right\} + \frac{2}{D_{c}} (J - 1) \tag{11}$$

where $\mu_c = \mu_{c1}$, $D_c = D_{c1}$ for $\sigma_{vm} < \sigma_{critical}$, $D_c = D_{c2}$ and $\mu_c = \mu_{c2}$ for $\sigma_{vm} \ge \sigma_{critical}$. F = RU is the polar decomposition of the deformation gradient where R is the rotation tensor and U is the stretch tensor.

Depending on the state of the stresses (before or after the critical value of the von Mises stress), the shear modulus μ_c is assigned the value of μ_{c1} and μ_{c2} and the stresses are updated according to Eq. (11). The VUMAT subroutine is verified against the built-in neo-Hookean material in Abaqus by setting $\mu_{c1} = \mu_{c2}$ and consistent results are obtained.

The third model to study the softening effect in the \mathcal{C} -phase employs a viscoelastic consideration for describing its mechanical response. The instantaneous response of the lipid model at t=0 is still assumed to be neo-Hookean and is captured by Eqs. (2) and (6). Viscoelasticity leads to the relaxation of the shear modulus which is described through a single term Prony series: $\mu_{\varepsilon}(t) = \mu_{\varepsilon}(\infty) + (\mu_{\varepsilon}(0) - \mu_{\varepsilon}(\infty))e^{-t/\tau_R} = \mu_{\varepsilon}(0) * g_R(t)$, where $g_R(t)$ is the dimensionless relaxation function: $g_R(0) = 1$ and $g_R(\infty) = \mu_{\varepsilon}(\infty)/\mu_{\varepsilon}(0)$. The built-in viscoelastic model in Abaqus is utilized to model the continuous phase for this approach in which the stress–strain relationship is of the following form:

$$\tau = \tau_0 + dev \left[\int_0^t \dot{g}_R(s) \bar{F}_t^{-1}(t-s) . \tau_0(t-s) . \bar{F}_t^{-T}(t-s) ds \right]$$
 (12)

where $\tau = dev(J\sigma)$ is the deviatoric part of the Kirchhoff stress and $\tau_0(t)$ is the deviatoric part of the instantaneous stress derived from the neo-Hookean strain energy function. A relative deformation gradient $F_{t-s}(t) = \frac{\partial x(t)}{\partial x(t-s)}$ is used to map the stress in the configuration at time (t-s) and time t.

In summary, the following material models are used to describe the monolayer: the domain is modeled as a pure neo-Hookean material with shear and bulk moduli μ_d and $K_d \gg \mu_d$. The \mathcal{C} -phase is modeled using four numerical models. One, a pure neo-Hookean material with shear and bulk moduli μ_c and $K_c \gg \mu_c$. Two, an elastic-plastic model where the elastic part is described by a neo-Hookean behavior with shear and bulk moduli μ_c and $K_c \gg \mu_c$ and plasticity occurs when the yield stress σ_{yl} is reached. Three, a bielastic model based on a piecewise neo-Hookean energy function where the shear modulus is softened from μ_{c1} to μ_{c2} when the von Mises stress surpasses a critical value. The bulk moduli K_{c1} and K_{c2} are larger than the shear moduli to enforce quasi-incompressibility. Four, a viscoelastic model where the shear modulus $\mu_c(t)$ relaxes over time.

The following sets of material parameters were used in the simulations. The ratio between the shear moduli of domain and the continuous phase $\frac{\mu_d}{\mu_c} \approx 25$ as the domain is stiffer than the matrix. The ratio between the bulk and shear moduli $\frac{K}{\mu}$ is set to be 20 to enforce quasi-incompressibility (Dassault Systèmes, 2018) which correspond to an equivalent Poisson ratio of 0.475. The dimensionless ratio between the critical stress for the onset of plasticity or softening in bielastic material model is set to be $\frac{\sigma_{yl}}{\mu_c} = \frac{\sigma_{critical}}{\mu_c} \approx 1.6$. The ratio $\frac{\mu_{cl}}{\mu_{c2}}$ between the moduli of the continuous phase for the bielastic case is varied from 1 to 50 to test the effects of material softening on the shear banding mechanism in the monolayer. Six specific cases of this ratio are presented $\frac{\mu_{cl}}{\mu_{c2}} = 1, 2, 5, 10, 20, 50$.

3. Experimental results

Lipid monolayers are studied at multiple length scales. Absent in the literature is a formal framework to define this multiscale structure. Here, we aim to provide a framework for the scale space of lipid monolayers. Fig. 1A shows the schematic setup for Langmuir monolayer experiments. The entire lipid covered surface forms the monolayer with a length scale on the order of 1×10^5 µm; we will term this the geometric outer scale of the system.

Two forms of data are often obtained at the monolayer outer scale: surface pressure (Π), defined as the difference between the surface tensions of pure water and lipid covered interface ($\Pi = \gamma_o - \gamma$), and an image (\mathcal{M}) (see Fig. 1). In both cases, it is customary to assume that the monolayer at the outer scale is a uniform two-dimensional manifold \mathcal{M} embedded in three-dimensional space R^3 .

3.1 Image analysis

Fluorescence images, acquired at different area fractions during the compression and expansion of the monolayer (see Fig. 1B), provide a resolution of the spatial structure of the monolayer at the scale of a few micrometers. At low surface pressures with the monolayer in the liquid expanded (LE) phase, the fluorescent probe TR-DHPE is homogeneously mixed in with the lipids, and FM imaging does not resolve any structure. Structure first appears in the images upon nucleation of liquid condensed (LC) domains. Throughout the LE-LC phase transition the LC domains grow in size. The domains appear dark in FM images because the bulky headgroup of TR-DHPE is excluded from the well-ordered crystalline packing structure. However, beyond a certain compressive strain the LC domain growth stops. Often in the monolayer literature, a tremendous amount of interpretation is made about the structure and location of given lipid components and their properties simply from FM images. We will refrain from making such leaps of scientific faith. From the vantage of scale space, the FM data simplify to binary pictures with dark regions (D-phase) and bright regions $(C_{EM}$ -phase). We will refrain from using LE and LC, because these definitions convolute mechanical properties with imaging data, yet the former cannot be extracted from the latter at this scale. The data structure from the FM images can formally be defined as $\mathcal{D} \cup \mathcal{C}_{FM} \in \mathcal{M}$. $\mathcal{D} \cup \mathcal{C}_{FM}$ can be studied from a geometric and topologic standpoint. Indeed, as will be detailed later, a particular geometric rearrangement of $\mathcal{D} \cup \mathcal{C}_{FM}$ is at the heart of this paper, the so-termed banding instability (Pocivavsek, Frey, et al., 2008).

Before considering banding in detail, one last data feature is often seen and described at the level of \mathcal{M} : collapse. In the lipid monolayer literature, collapse has a thermodynamic and imaging definition. In terms of monolayer thermodynamics, collapse is traditionally defined as the point where the isotherm becomes horizontal at a high lipid packing density. By taking the derivative of the isotherm, one can interpret collapse as a zone of infinite compressibility. Often this point in the isotherm is correlated with the

FM image structure on the monolayer. Fig. 2 shows the first ever generalized collapse phase diagram based on the structure of the collapsed monolayer as derived from FM images. Without loss of generality, we can interpret collapse as the loss of the planar geometry of \mathcal{M} . More formally, $\mathcal{M} = \bigcup_{i=1}^{\ell} T\mathcal{M}_i$, where $T\mathcal{M}_i$ defines a chart domain composed of the local tangent space isometric to the plane; the entire monolayer is given by gluing the different $T\mathcal{M}_i$ together to form the atlas \mathcal{M} . The process of defining scale space involves defining the different layers of local charts giving rise to atlases

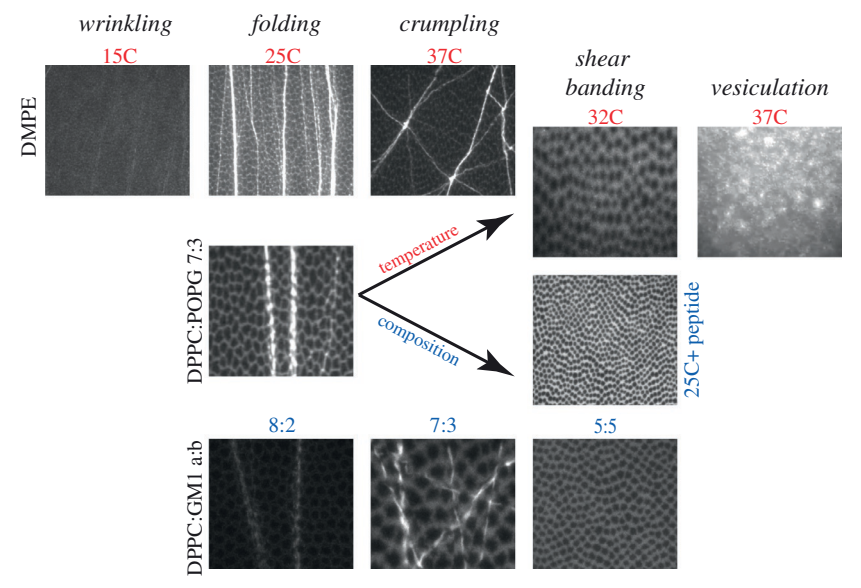


Fig. 2 Generalized monolayer collapse phase diagram showing the richness of collapse states in lipid monolayers and their tunability with various field parameters including composition and temperature. Monolayer collapse is an elastic instability whereby the lipid membrane collectively over some length scale undergoes in-plane or out-ofplane displacement. This is a fundamentally different mode than movement of small clusters of lipids from the surface to the bulk phase well described by Gibbs' absorption monolayers. The collective collapse modes are inherently governed by membrane elasticity. Several of the authors have explored the inextensible membrane limit of monolayer collapse via wrinkling and folding where plate-like bending modes dominate (Diamant et al., 2001, 2000; Pocivavsek, Dellsy, et al., 2008; Pocivavsek et al., 2009). Relaxation of membrane inextensibility leads to multidirectional folding and eventually the shear banding mode of in-plane relaxation (Pocivavsek, Frey, et al., 2008). In this paper, we explore the general framework in which in-plane membrane elasticity can be modeled. This figure demonstrates that the different collapse modes are universal, spanning several different lipid compositions. Furthermore, membrane instability can be controlled either by changing composition with the addition of peptides or unsaturated lipids or by temperature in single component systems.

which become a large scale chart again leading to a new atlas on a different scale. Working at the outer scale of \mathcal{M} , before collapse, $\ell \to 1$ because the monolayer is everywhere isometric to the plane defined by the air/water interface, as such one chart gives the whole atlas. Collapse forces us to redefine the above partition into multiple charts; as such at its most fundamental topologic level, collapse can be viewed as the break-up of the monolayer tangent space from a single vector space into multiple vector spaces, thereby defining a monolayer tangent bundle TM. Nonzero curvature of the tangent bundle defines collapse. If we define a local metric parameterization of the monolayer, collapse by these definitions can be studied using standard methods of differential geometry. Indeed, the canonical collapse structure studied in the literature is the wrinkle-to-fold instability (Pocivavsek, Dellsy, et al., 2008; Pocivavsek, Frey, et al., 2008), where the projected one-dimensional monolayer collapses via buckling (appearance of curvature). Measurement of amplitudes from FM images is experimentally impossible. However, the position of the local monolayer surface is often defined through intensity level sets in the FM images, increasing brightness is correlated to higher lipid density in the planes normal to the air/water interface (see Diamant et al., 2001, 2000 for detailed discussions). Qualitatively this allows us to identify bright regions in Fig. 2 as regions of nonzero TM curvature, i.e., collapse.

No standard geometric or topologic language exists to define the different collapse states. As such, we use descriptive terms in Fig. 2: wrinkling, folding, crumpling, shear banding, and vesiculation. The generalized collapse phase diagram shows that both temperature and composition can be used to tune the type of collapse a monolayer will undergo. Monolayers of varying lipid compositions and at different temperatures can all have very similar collapse structures on the scale of \mathcal{M} . This supports the existence of a generality not only of geometry and topology but also mechanism in lipid monolayer collapse.

The characterization of collapse geometry is the first step before any discussion of mechanism can be undertaken. As noted above, on the outer scale, the geometry of \mathcal{M} can be studied by studying the structure of $\mathcal{D} \cup \mathcal{C}_{FM}$. The operationalization of this was undertaken in our prior work on lipid monolayer banding (Pocivavsek, Frey, et al., 2008). First, the FM image is binarized, followed by the calculation of the image autocorrelation function $\langle \rho(x_{m,n}), \rho(x_{m+i,n+j}) \rangle$. Taking the Fourier transform of the autocorrelation function gives the image structure factor S(q). Fig. 3 shows the outline of this approach and its application to distinguishing two collapse states: folding and banding. For monolayers which fold, S(q) remains overall

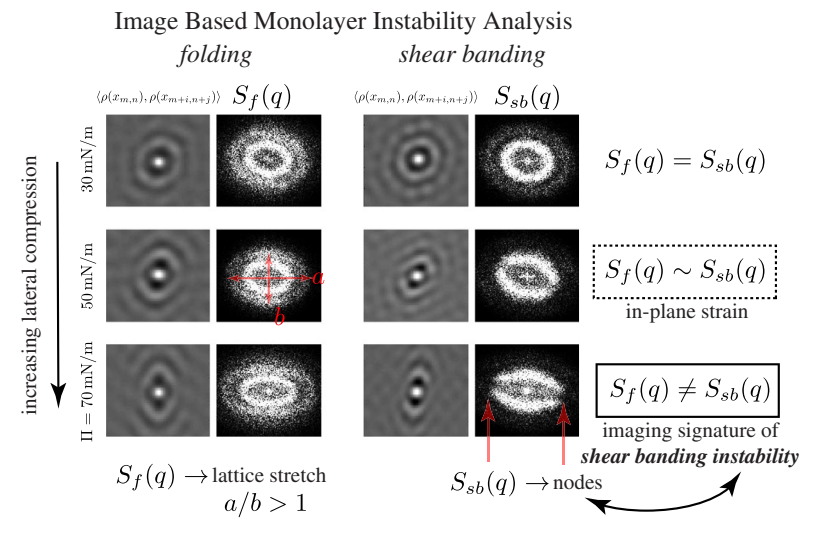


Fig. 3 Geometric in-plane monolayer instabilities are captured by calculating the per-pixel image autocorrelation function $\langle \rho(x_{m,n}), \rho(x_{m+i,n+j}) \rangle$, whose Fourier transform gives the image structure factor S(q). In our prior experimental work on lipid monolayer banding (Pocivavsek, Frey, et al., 2008), we discovered a correlation in the appearance of nodes in S(q) and the banding instability. In monolayers which fold, $S_f(q)$, at high pressures, becomes distorted, indicating overall lattice shearing, but does not show nodes. The appearance of nodes in $S_{sb}(q)$ indicates the loss of in-plane stability. This general method can be applied to experimentally and computationally derived data.

constant throughout compression, minus some local distortion which can be correlated to global monolayer stretching in the direction normal to compression but in-plane. Because the image is made binary, this analysis cannot capture variation in local intensity level sets, as such actual folds cannot be captured. In monolayers which undergo banding, S(q) changes structure with increasing compression. As Fig. 3 shows, the symmetric S(q) develops nodes as banding occurs. Studying S(q) proves to be a useful measure of geometry on the outer scale of \mathcal{M} . Later, we apply this method to computationally derived monolayer structures.

This completes our analysis of the outer scale of the lipid monolayer scale space. From the standpoint of collapse, we see that monolayers that fold show very few identifiable geometric features in \mathcal{M} until the folds appear. However, monolayers which undergo in-plane banding show a rich set of geometric features in \mathcal{M} . The next step in our analysis is to probe the geometry of the monolayer at a higher spatial resolution, "de-blurring" scale space and defining a submanifold \mathcal{M}_{AFM} . As outlined in Section 2, this is accomplished by transferring the monolayer from the air/water interface onto a

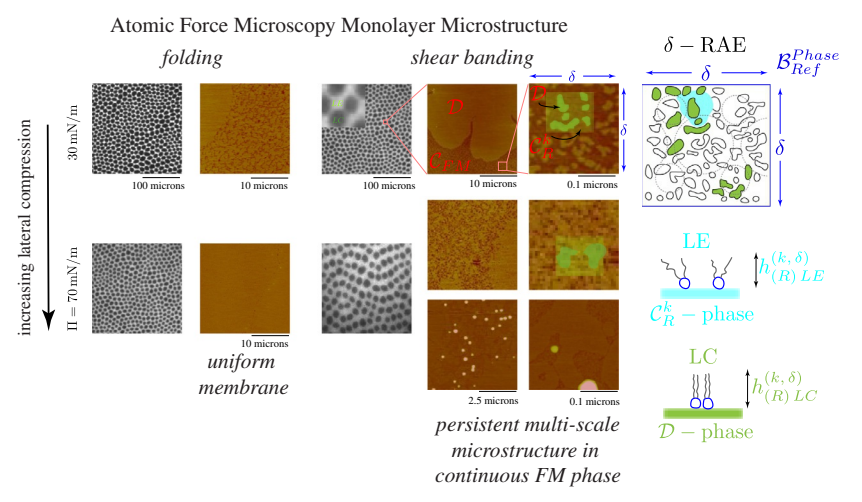


Fig. 4 Lipid monolayers show a rich multiscale structure in-plane and out-of-plane. At the completion of the LE–LC phase transition plateau (see Fig. 1B), the monolayer has a biphasic appearance with dark circular domains (LC or \mathcal{D}) surrounded by a bright continuous phase (LE or \mathcal{C}_{FM}). Continuity of the two phases in the FM images is blurred to order of pixel size. When these monolayers are evaluated on a smaller length scale using AFM, a new set of structures appears in the \mathcal{C}_{FM} phase, which is composed of submicron \mathcal{D} -phase domains of height $h_{(R)LC}^{(k,\delta)}$ which is equal to the height of the large-scale circular domain. The submicron \mathcal{D} -phase domains are surrounded by a continuous \mathcal{C}_R^k -phase with a lower height $h_{(R)LE}^{(k,\delta)}$. Our data show that upon increasing surface pressure to collapse, monolayers which undergo folding transition do so while maintaining a uniform height in the membrane; however, monolayers which undergo banding have a persistent multiheight and in-plane multiscale structure. The figure highlights the different phases in the AFM images, which will be referenced in the theoretical part of the paper.

solid substrate and performing AFM. Fig. 4 shows a set of FM images and the corresponding AFM images for representative monolayers which collapsed by folding and banding. The AFM data have richer structures compared to the FM images. The data are still in the form of images; however, the intensity at each pixel is directly correlated to local distance normal to the image plane. Recall in the FM images, the intensity distribution allows different domains \mathcal{D} and \mathcal{C}_{FM} to be defined; however, no direct experimental correlation between intensity and other length scales exists. Thus with AFM, there is a higher resolution lateral scale and the appearance of a quantifiable height scale. As Fig. 4 shows, brighter regions of the AFM image correspond to thicker areas of the monolayer. These areas also are easily identifiable as the dark domains in the FM images, as such we will continue to refer to this phase as the \mathcal{D} -phase which now has a corresponding height $h_{(R)LC}^{(k,\delta)}$.

The darker regions in the AFM images correspond to a lower height phase. When the FM and AFM data for the continuous \mathcal{C}_{FM} -phase are compared, we observe the appearance of a new geometry at the AFM scale. Stated formally in terms of geometric space, $\mathcal{D} \in \mathcal{M}_{AFM} \equiv \mathcal{D} \in \mathcal{M}$ but $C_{AFM} \in \mathcal{M}_{AFM} \neq C_{FM} \in \mathcal{M}$. When one looks into the C_{AFM} -phase, we see an almost self-similar geometry to the original global geometry $\mathcal{D} \cup$ $\mathcal{C}_{FM} \in \mathcal{M}$ except on a much smaller inner and outer scale. We define this new higher resolution doubly embedded geometry as $\mathcal{D} \cup \mathcal{C}_R^k \in \mathcal{C}_{AFM} \in$ \mathcal{M}_{AFM} . We also link a height $h_{(R)LE}^{(k,\delta)}$ to the \mathcal{C}_R^k -phase. Increasing lateral compression causes a change in the C_{AFM} -phase geometry. For both monolayers that fold and band, increasing lateral compression causes a decrease in area coverage of the C_R^k -phase. For monolayers that fold, at the end of compression just before folding onset, the $\mathcal{C}^k_{\scriptscriptstyle R}$ -phase has disappeared and only a uniform height \mathcal{D} -phase remains. However, for monolayers which band, $\mathcal{D} \cup \mathcal{C}_R^k \in \mathcal{C}_{AFM}$ phase persists to even high pressures, the mechanical implications of this are explored in the theoretical section of this paper.

This completes the geometric analysis of scale space for lipid monolayers. The more formalized geometric approach used here allows us to define and study not only the geometry but also topology of lipid monolayers and their mechanical instabilities. Such approaches have led to wonderful insights in the behavior of three-dimensional liquid crystal phases (Safran, 1994), but are lacking for lipid monolayers. Several observations are noteworthy. First, between the two collapse modes analyzed, the dynamics portions of the geometry switch. In \mathcal{M} , the folding monolayer is geometrically static while the banding monolayer shows geometric evolution; however, in \mathcal{M}_{AFM} , the folding monolayer shows more rapid evolution with the complete disappearance of \mathcal{C}_R^k with compression, while the banding monolayer geometry stays more static. Second, because of the different levels of information in the image-based data at different scales notions of continuity and homogeneity become complex.

3.2 Isotherm analysis

From the standpoint of thermodynamics, the uniformity of monolayer response is taken as given when compression isotherms are measured. However, beyond a certain surface packing density, the measured surface pressure is likely only representative of a submanifold of (\mathcal{M}) (Pocivavsek, Frey, et al., 2008; Witten, Wang, Pocivavsek, & Lee, 2010). To prove this, consider that the Wilhelmy plate is the standard method for monitoring

interfacial pressure in a Langmuir trough; it consists of a rectangular strip connected to a force transducer (see Fig. 1A). The meniscus at the air/ lipid/water interface pulls down the strip with a force proportional to the net surface tension. In the case of \mathcal{M} , under static conditions, the surface pressure is uniform and unaffected by the geometry of the meniscus. As the monolayer is compressed, surface phase transitions occur and the fluid monolayer transitions to a solid one. Working with an ideal system where the monolayer transitions from a perfect fluid to a perfect solid but geometrically remains a smooth two-dimensional manifold \mathcal{M} , we investigate the impact on the output of the Wilhelmy measurement. We take the ability to sustain a static shear stress as the only difference between liquid and solid monolayers. \mathcal{M} is taken as a thin annular disk of outer radius R and inner radius a. The inner boundary represents the Wilhelmy plate; the outer radius represents the boundary of the Langmuir trough or external length. Applying a uniform compressive radial displacement field u(r) generates a radial strain $\gamma_{rr} = \partial_r u$ and an azimuthal strain $\gamma_{\phi\phi} = u/r$. Assuming linear elasticity, the strain gives rise to a proportional stress σ with the same principle axes. $\sigma_r = A \gamma_r +$ $B\gamma_{\phi\phi}$ and $\sigma_{\phi\phi} = B\gamma_r + A\gamma_{\phi\phi}$. The equation of equilibrium is given by $\partial_i\sigma_r =$ $(\sigma_{\phi\phi} - \sigma_n)/r$ (see derivation in Witten et al., 2010). Substituting the stresses for a uniform radial displacement gives $\partial_r^2 u + \partial_r u/r - u/r^2 = 0$. The general solution is given by $u(r) = C[r + b^2/r]$ (Witten et al., 2010). Making the appropriate substitutions gives $\sigma_{rr} = AC[(1 + B/A) - (b/r^2(1 - B/A))]$ and $\sigma_{rr} + \sigma_{\phi\phi} =$ 2C(A+B), which represents the hydrostatic stress. Several insights come from this analysis. In the setting of a perfect liquid monolayer A = B, since no deviatoric stresses are possible under static conditions, and there is no dependence of the stress on location from the inner boundary, b = r. In this case, the thermodynamic measurement is uniform and valid over \mathcal{M} . However, presume B < A, which might occur for an elastic film. In this case, the radial stress will reverse sign whenever $b/a > \sqrt{(1+B/A)/(1-B/A)}$. Now a new inner scale appears: $b \sim a\sqrt{(1+B/A)/(1-B/A)}$. To accurately sample the surface pressure, one would have to do so on the submanifold $\mathcal{M}_b \subset \mathcal{M}$. This simple example serves to show that even the much used and measured isotherm is sensitive to the multiscale construction of the monolayer. There are currently no established methods on how to precisely define the submanifold \mathcal{M}_b at which the lipid monolayer can be considered a uniform continuum solid from the standpoint of elastic response.

With the above limitations of local surface pressure measurements in mind, it is possible to obtain effective elastic moduli from isotherm measurements (see Fig. 5). The two-dimensional bulk modulus K is related to the

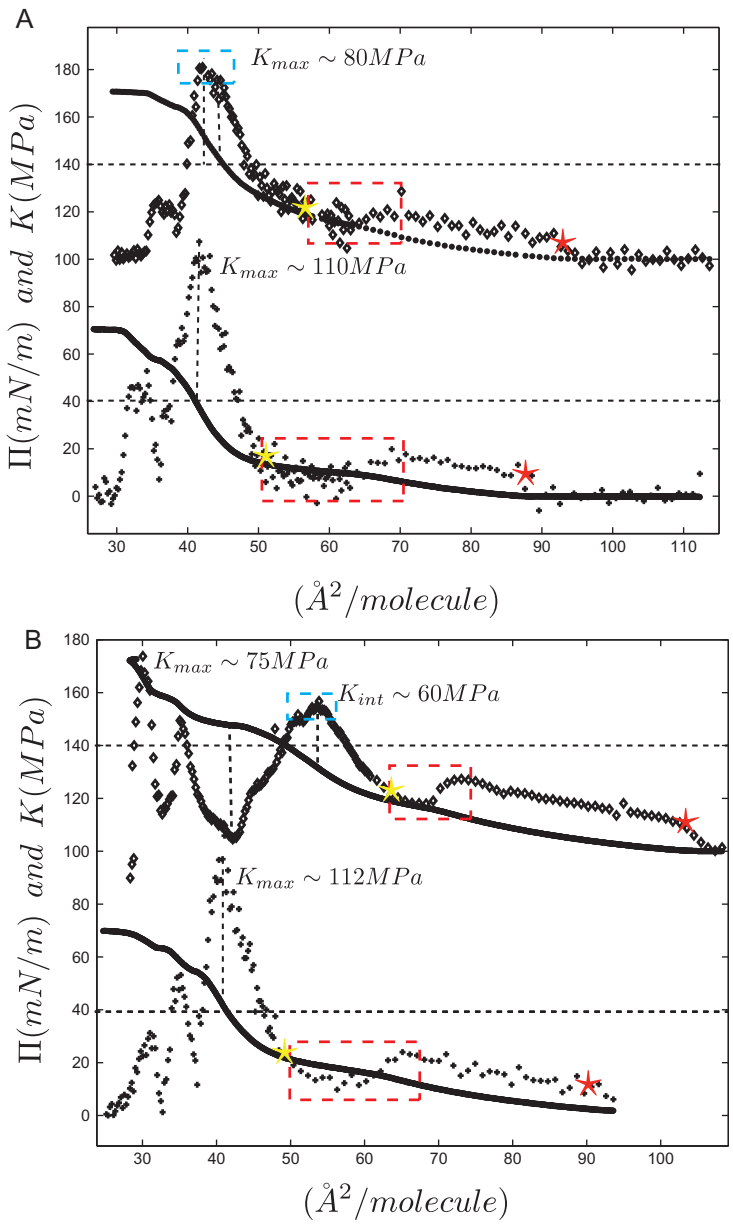


Fig. 5 (A) *Bottom curve* is DPPC:GM1 8:2, *top curve* is DPPC:GM1 5:5 displaced 100 points on *y*-axis. In both curves, the *red box* marks the LE to LC phase transition and the *yellow* \star the rigidity onset point. In the case of DPPC:GM1 8:2, where no in-plane rearrangement occurs, $K_{max} \sim 110$ MPa is reached at 40 mN/m at an area per molecule (*Continued*)

slope of the $\Pi - A$ isotherm, $K_{2D} = -A \frac{\partial \Pi}{\partial A}$. Dividing K_{2D} by the given monolayer thickness ($h \sim 2 \text{ nm}$) gives the traditional bulk modulus K by simple dimensional analysis (Gopal, Belyi, Diamant, Witten, & Lee, 2006; Gopal & Lee, 2001; Pocivavsek, Frey, et al., 2008). At high area per molecule, the monolayer is liquid and the compressibility is high, marked by a low K (long nearly horizontal lines in the data). The LE–LC phase transition plateau is marked by a discontinuity and drop in K. It is tempting to quantitatively interpret this from a mechanistic standpoint of phase transitions and area condensation occurring on a much smaller scale; however, given the analysis above about the validity of Π in an ill-defined subdomain \mathcal{M}_b , we believe it is more appropriate to simply interpret this inflection as a sign of dissipation but not link to any particular mechanism. Following the LE-LC phase transition, as defined via imaging on \mathcal{M} , K undergoes a steep rise until a sharp inflection is again reached followed by a complex region of decline and oscillating *K* values. This indicates that the monolayer never truly reaches a mechanically stable state post LE-LC phase transition, given that even for very small compression the magnitude of K changes. Again, given that the isotherm is only providing information locally in \mathcal{M}_b while the displacement field is being applied globally on \mathcal{M} , any mechanistic interpretation is difficult. It is clear however that a maximum K is reached far before collapse is seen on the scale of FM images. This indicates that some local dissipation or relaxation is occurring that is not captured in the FM scale space.

Fig. 5—cont'd of \sim 40 (Ų/molecule). The transition in this case is very sharp. In the case of DPPC:GM1 5:5, where the monolayer undergoes an in-plane domain rearrangement, $K_{max} \sim 80$ MPa is reached at a slightly higher surface pressure of 50 mN/m, however, at a similar area per molecule of \sim 40 (Ų/molecule). (B) The *bottom curve* is DPPC:POPG 7:3, while the *top curve* is DPPC:POPG:SP-B 9-25 70:30:2. The phase transition at low molecular density and the rigidity onset points are marked as above. In the *bottom curve*, where there is no peptide and the monolayer does not rearrange, $K_{max} \sim 112$ MPa is reached at 40 mN/m at an area per molecule of \sim 40(Ų/molecule). In the monolayer with the peptide, a first maximum is reached earlier at 31 mN/m and 54 (Ų/molecule). The monolayer begins to relax at this point. This is likely due to a conformational change in the peptide, at the start, and later on a transition of the peptide from the surface into the subphase.

4. Finite element analysis

We present a highly novel method of integrating experimentally derived geometry with finite element analysis (FEA) to model lipid monolayer response under compression. In our prior work, we postulated the banding relaxation was qualitatively a "soft shear relaxation" triggered by a stress-induced instability (Pocivavsek, Frey, et al., 2008). Until the present work, this remained only a hypothetical notion, as we did not have a theoretical or computational model to validate it. Fig. 6 details our current workflow. As detailed above, at the scale space of FM images \mathcal{M} , the banding instability is defined as a change in the image structure factor S(q). To build the initial computational geometry, we map the distribution of domains at the end of the LE–LC phase transition plateau from ${\cal M}$ into a computational submanifold \mathcal{P} . From the standpoint of geometry, \mathcal{P} preserves the exact shape of the \mathcal{D} -phase domains and their initial positions relative to each other. We then define the C_{FM} -phase as $\mathcal{P} - \mathcal{D}$. Staying true to the FM scale space, $\mathcal P$ has uniform thickness, which implies $h_{(R)LE}^{(k,\delta)}=h_{(R)LC}^{(k,\delta)}$ The goal of these simulations is to provide a computational framework with which to uncover the necessary conditions within the continuum mechanical limit for lipid monolayer banding.

Lipid monolayer collapse has traditionally been viewed as a continuum instability, though there lacks a uniform and general theory to explain the various observed collapse modes (see Fig. 2). Of all the collapse modes, folding has received the greatest attention in the literature (Diamant et al., 2001, 2000; Lipp et al., 1998; Pocivavsek, Dellsy, et al., 2008; Pocivavsek et al., 2009). There is a clear consensus that folding is a continuum monolayer instability that is dominated by elasticity. The dominant length scale of monolayer folds is explained by a very simple linearly elastic model of thin film buckling (Pocivavsek, Dellsy, et al., 2008). This motivates our approach in building a computational model for monolayer banding. Given plate theory explains folding to first order, and linear plate theory dictates suppression of in-plane modes in favor of buckling while banding suppresses folding; building a model that can capture in-plane rearrangement of the \mathcal{D} -phase is critical. As detailed in Section 2, we model the \mathcal{D} -phase as a stiffer hyperelastic continuum. We vary the constitutive response of the C_{FM} -phase. If \mathcal{C}_{FM} responds elastically like a neo-Hookean material, strain develops predominantly in the direction normal to compression spanning different

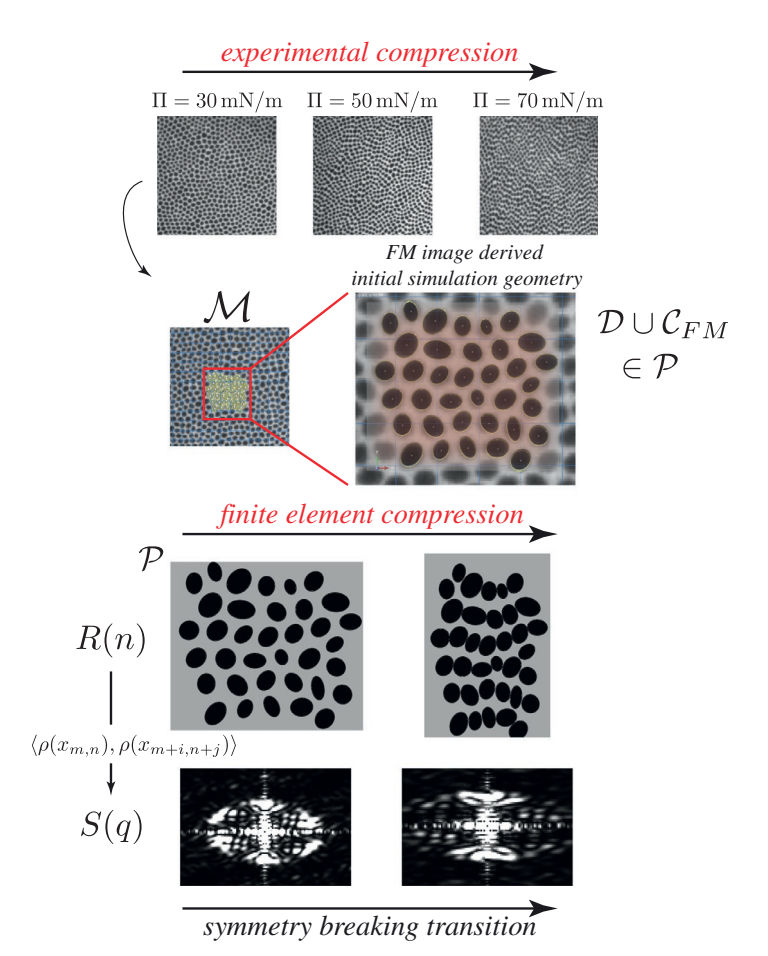


Fig. 6 Fluorescent microscopy images at lower surface pressures are used to generate input geometries for finite element modeling of a local portion of the lipid monolayer at the FM-scale. The \mathcal{D} -phase domains are segmented as separate individual parts (*black domains*) embedded in the continuous \mathcal{C}_{FM} -phase (*gray background phase*) making a submanifold \mathcal{P} , where $\mathcal{P} \subset \mathcal{M}$, with \mathcal{M} representing the entire monolayer. We do not at this point geometrically model the smaller length-scale structure contained in the \mathcal{C}_{FM} -phase composed as a union of the \mathcal{C}_R^k -phase and \mathcal{D} -phase microdomains. However, the effect of this microstructure comes into the problem at the level of the constitutive response of the \mathcal{C}_{FM} -phase. Outputs of FEA simulations, where the initial patch is compressed along the horizontal direction mimicking the Langmuir trough loading geometry, are shown. S(q) is calculated from the real-space R(n) images showing that initially the \mathcal{D} -phase domains within this local monolayer patch form a perfect hexagonally close-packed structure. The appearance of the symmetry breaking transition signified by nodes in S(q) and bands in R(n) demonstrates that the banding instability can be captured in FEA, reproducing what is seen in experiments.

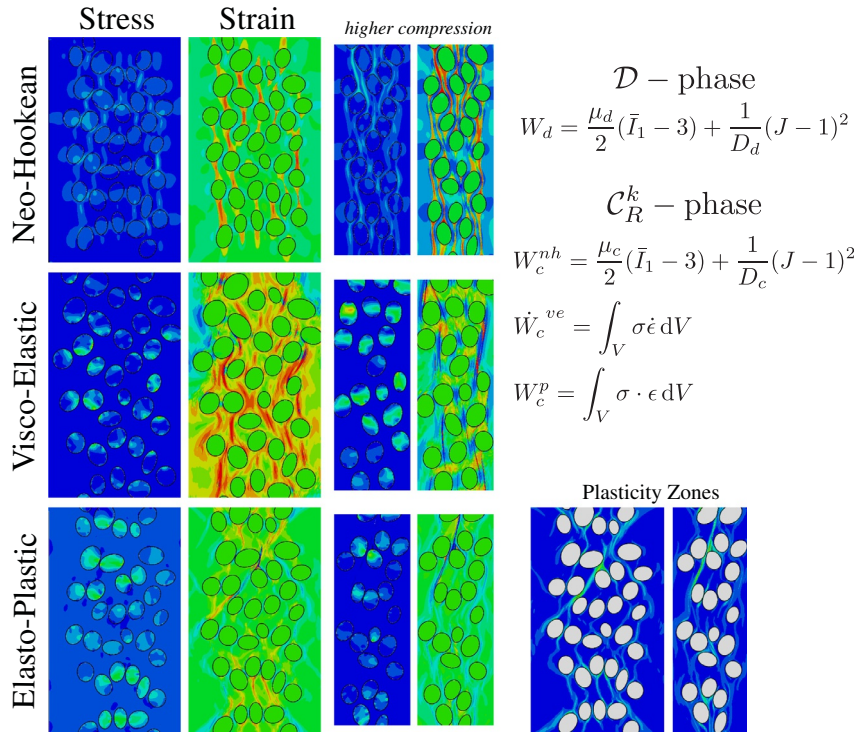


Fig. 7 Finite element modeling of \mathcal{P} under lateral compression is carried out using a neo-Hookean hyperelastic energy functional for the \mathcal{D} -phase and three built-in constitutive models for the \mathcal{C}_R^k -phase: neo-Hookean, viscoelastic, and elasto-plastic. If both phases respond elastically (*top row*) then even at very high compressions, the monolayer distorts but does not undergo banding. For the two dissipative constitutive models, signatures of banding clearly appear; these are more present in the case of plasticity than viscoelasticity. Because the \mathcal{D} -phase is stiffer than the \mathcal{C}_R^k -phase, the stress field is primarily seen in the \mathcal{D} -phase (*first column*). However, the \mathcal{C}_R^k -phase contains the majority of the strain. In the case of neo-Hookean and viscoelastic responses, the strain is predominantly tensile and normal to the direction of compression, indicating that incompressibility of \mathcal{P} dictates the strain field. In the case of plasticity, localized zones of high shear appear throughout the \mathcal{C}_R^k -phase. These zones are tilted at $\sim \pi/4$ rad to the axis of compression and correspond to local regions of high plastic deformation and dissipation. Moreover, the appearance of these dissipation zones in the \mathcal{C}_R^k -phase correlates to the reorganization of the \mathcal{D} -phase into bands (see *bottom right*).

domains (see Fig. 7 top row). This strain distribution persists to even high lateral compressions. If we allow for dynamic dissipation in C_{FM} by modeling it as a viscoelastic solid, a more complex and uniformly distributed strain pattern develops. In both the neo-Hookean and viscoelastic cases, the

distribution of the \mathcal{D} -phase in R(n) does not show banding. If we allow for stress dissipation in the form of plasticity (see last column in Fig. 7), localized zones of high shear stress appear tilted at an angle $\sim \pi/4$ rad to the axis of compression. These shear bands correspond to regions of active plastic deformation. Moreover, the geometry of the deformed configuration in \mathcal{P} shows banding in R(n) as well as the appearance of nodes in S(q) at high lateral compression (see Fig. 6).

The simulations presented in Fig. 7 prove that for banding to occur a degree of dissipation is needed in the \mathcal{C}_{FM} -phase. We investigated nonelastic forms of dissipation such as viscoelasticity and plasticity. Experiments (see general collapse phase diagram in Fig. 2) show that banding represents an evolution of elastic monolayer response with increased degrees of freedom in-plane. Elasticity without dissipation has successfully explained monolayer folding (Pocivavsek, Dellsy, et al., 2008; Pocivavsek et al., 2009). There is no experimental evidence that the monolayer has more complex constitutive properties such as viscoelasticity or plasticity in the banding regime. Fig. 4 shows that the local substructure within the C_{AFM} -phase given by the distribution and proportion of the $\mathcal{D} \cup \mathcal{C}_{R}^{k}$ -phases is the only experimental evidence of a difference between monolayers that fold and those that band. The central hypothesis of this paper is that a purely elastic source of dissipation can lead to the banding instability. The theoretical portion of this paper builds a constitutive model for $\mathcal{D} \cup \mathcal{C}_R^k \in \mathcal{C}_{AFM} \in \mathcal{P}$ using the AFM derived data as presented in Fig. 4. This model predicts the existence of an internal elastic instability arising from the microstructure within the \mathcal{C}_R^k phase. To model this with FEA, we construct a bielastic strain energy for the C_R^k -phase: $W_c = \frac{\mu_{c1}}{2}(\bar{I}_1 - 3) + \frac{1}{D_1}(J - 1)^2$ for $\sigma_{vm} < \sigma_{critical}$ and $W_c =$ $\frac{\mu_{c2}}{2}(\bar{I}_1-3)+\frac{1}{D_{c2}}(J-1)^2$ for $\sigma_{vm}\geq\sigma_{critical}$. The \mathcal{D} -phase is modeled as a uniform elastic solid defined by a single shear modulus μ_d . Three dimensionless ratios are held constant: first, a constant ratio between the shear moduli of domain and the continuous phase $\frac{\mu_d}{\mu_c} \approx 25$; second, a fixed ratio between the bulk and shear moduli $\frac{K}{\mu}$ = 20 enforcing quasi-incompressibility; and third, a fixed ratio between the critical stress for the onset of softening in a bielastic material model $\frac{\sigma_{yl}}{\mu_{\epsilon}} = \frac{\sigma_{critical}}{\mu_{\epsilon}} \approx 1.6$. This allows us to study the effect of different levels of softening by adjusting the ratio μ_{c1}/μ_{c2} . Six specific cases of this ratio are simulated $\frac{\mu_{c1}}{\mu_{c2}} = 1, 2, 5, 10, 20, 50$. Note that when $\mu_{c1}/\mu_{c2} = 1$, the continuous phase becomes a pure neo-Hookean material. Fig. 8 shows the distribution of the \mathcal{D} -phase at low and high lateral compression as a function of $\frac{\mu_{cl}}{\mu_{o}}$; for comparison, we include the elasto-plastic model in the last column.

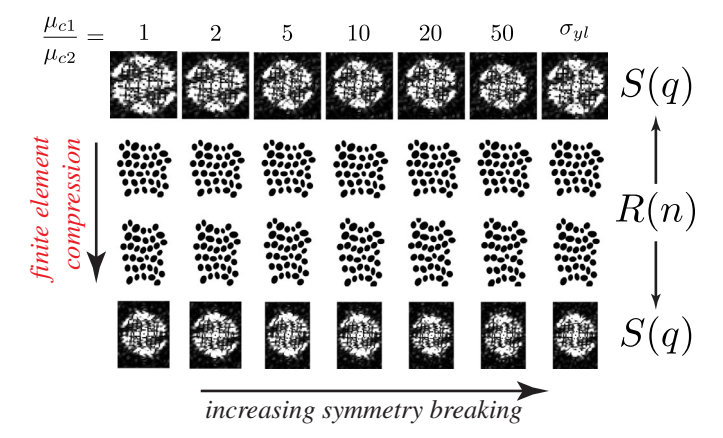


Fig. 8 To test the hypothesis that purely elastic sources of dissipation can lead to the banding instability FEA simulations are performed with a bielastic strain energy for the \mathcal{C}_R^k -phase: $W_c = \frac{\mu_{c1}}{2}(\bar{l}_1 - 3) + \frac{1}{D_{c1}}(J - 1)^2$ for $\sigma_{vm} < \sigma_{\text{critical}}$ and $W_c = \frac{\mu_{c2}}{2}(\bar{l}_1 - 3) + \frac{1}{D_{c2}}(J - 1)^2$ for $\sigma_{vm} \ge \sigma_{\text{critical}}$ (see main text for more details). By adjusting the ratio μ_{c1}/μ_{c2} , different levels of softening effects are examined, increasing left to right in the figure. Note that when $\mu_{c1}/\mu_{c2} = 1$, the continuous phase becomes a pure neo-Hookean material. For comparison, we include the elasto-plastic model in the *last column*. Each simulation is analyzed using the methods presented above, the real space image R(n) is transformed into the structure factor S(q). A low level and high level of lateral compression are analyzed, with results shown in the *top* and *bottom* two rows, respectively. For all cases, at low compressions, the \mathcal{D} -phase in \mathcal{P} is organized into a nearly perfect hexagonal close-packed structure. As lateral compression is increased, we see a transition to banding in R(n) and the appearance of nodes in S(q) that become most prominent for $\mu_{c1}/\mu_{c2} = 50$ and in the case of plasticity.

We calculate S(q) for each set of computationally derived domain images. At low compression, $\frac{\mu_{c1}}{\mu_{c2}}$ does not impact domain distribution and S(q) shows the \mathcal{D} -phase is organized into a nearly perfect hexagonal close-packed structure. As lateral compression is increased, we see a transition to banding in R(n) and the appearance of nodes in S(q) that become most prominent for $\mu_{c1}/\mu_{c2}=50$ and in the case of plasticity. This proves that banding can arise from a bielastic response in the \mathcal{C}_{AFM} -phase and is sensitive to the degree of softening dictated by the ratio μ_{c1}/μ_{c2} . The theoretical portion of this paper will provide an insight as to the source of this modulus ratio based on the \mathcal{C}_{AFM} -phase microstructure.

Fig. 9 shows the maximum and minimum principal strains in the C_{AFM} -phase at the same time points as the geometric analysis in Fig. 8. Since our analysis is constrained to relative ratios of certain moduli, the absolute magnitude of these strains is not to be interpreted too rigorously (we do

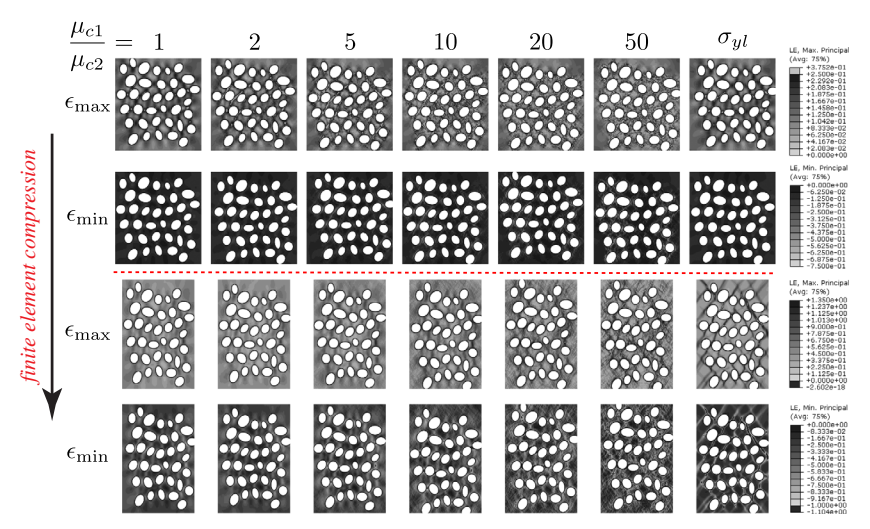


Fig. 9 The maximum and minimum principal strains in the \mathcal{C}_{AFM} -phase are analyzed for the two compression levels shown in Fig. 8 and the different values of μ_{c1}/μ_{c2} . The first column where $\mu_{c1}/\mu_{c2}=1$ corresponds to a pure neo-Hookean response, while the last column shows the strain distributions for the elasto-plastic system. At low compression (first two rows), the strain distribution is nearly homogeneous and equivalent in all cases. At higher compression, for low values of μ_{c1}/μ_{c2} , a predominantly tensile strain normal to the direction of compression develops. As μ_{c1}/μ_{c2} increases, this strain field begins to rotate such that by mismatch 20 and 50 strong shear bands appear very similar in distribution to the plastic shear bands. We take this as the hallmark signature of a local material instability in the bielastic response of the \mathcal{C}_{AFM} -phase leading to the global rearrangement of the \mathcal{D} -phase into bands.

provide the scales for completeness). The distribution of the strain however is informative, much as in Fig. 7. For the neo-Hookean case $\mu_{c1}/\mu_{c2} = 1$ up to $\mu_{c1}/\mu_{c2} = 10$, the maximum principal strain (tension) occurs between \mathcal{D} -phase domains in the direction normal to compression. This intuitively agrees with the notion that the quasi-incompressible monolayer when compressed laterally along the horizontal direction expands and is stretched vertically to conserve volume. Beginning at $\mu_{c1}/\mu_{c2} = 20$ and extending to mismatch 50, the vertically oriented tensile principal strain begins to rotate at higher compressions. The strain pattern which emerges in the bielastic materials is very similar to the plasticity zones seen earlier (see Fig. 7) and shown in the last column of Fig. 9. The appearance of these purely elastic shear bands arise from a local material instability in the bielastic response of the \mathcal{C}_{AFM} -phase leading to the global rearrangement of the \mathcal{D} -phase into bands.

5. Multiscale geometry of lipid monolayers

A basic asymmetry exists in monolayers, the hydrophilic headgroups bind with water molecules of the underlying subphase, upon which the hydrophobic tails stick out in air. Once the monolayer is formed, loading is applied by controlling the displacement of a (very slowly) moving rigid wall. The headgroups through contact tractions at the water-lipid interface bear the load. During this quasi-static process lipids undergo conformational and positional disarrangements. The former are well known to relate to

- (i) changes in conformations of the lipid tails (occurring with very negligible storing of energy compared with the energy stored within the water-headgroup layer), which undergo either shortening (through increase in "curliness" by rolling) or elongation, through unrolling their physical length,
- (ii) changes in the projection of the tails at the water-headgroup interface, which increases as shortening (and, sometimes, tilting) occurs.

The latter kind, i.e., positional disarrangements, involving switching of lipid clusters similar to jamming in granular materials (Hunt, Tordesillas, Green, & Shi, 2010; Majumdar, Krishnaswamy, & Sood, 2011; Majumdar & Sood, 2008; Tordesillas, Lin, Zhang, Behringer, & Shi, 2011; Tordesillas, Pucilowski, Lin, Peters, & Behringer, 2016), is envisioned to be a plausible mechanism for rearrangements of such clusters when material instabilities occurring through banding arise. This aspect will be discussed later. Other geometrical changes include the macroscopic deformation, describing the very slow motion of the headgroups within the water-lipid layer. Such deformation and along with positional disarrangements are captured through a multiscale kinematics based on the theory of Structured Deformations, labeled as SDs (Deseri & Owen, 2003, 2013, 2019), a relatively recent multiscale geometrical approach to the mechanics of complex bodies (a recent application to lipid bilayers, more precisely to the cell membranes, can be found in Carotenuto et al., 2020).

The multiscale geometrical changes discussed above are visualized in a time-snapshot of the lipid monolayer represented in four different configurations and displayed in Fig. 10. In the first three of such configurations, denoted as \mathcal{B}_{Virg} , $\mathcal{B}_{Ref}^{Phase}$, and $\mathcal{B}_{Ref}^{Posit}$, we consider a δ -Representative Area Element, labeled as δ -RAE, namely a small patch relative to the size of the whole monolayer. Indeed, the size $\delta \ll \ell$, where ℓ is the minimum

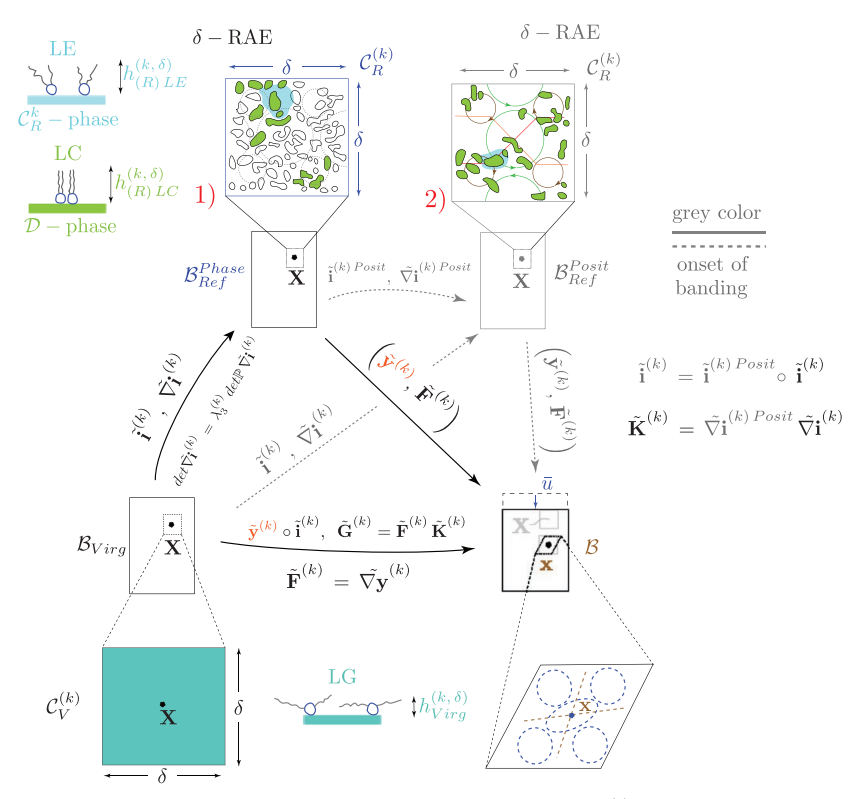


Fig. 10 Beginning in the lower left, the virgin configuration $\mathcal{B}^{(k)}_{Virg}$ is shown with a material particle \mathbf{X} within a smaller area of interest δ^2 , δ —RAE labeled $\mathcal{C}^{(k)}_{V}$. This configuration is homogeneous in height and lateral organization with no micro- or macrostructure; we label it LG. Through any sequence of mappings $\tilde{\mathbf{i}}^k$, $\mathcal{B}^{(k)}_{Virg}$ is taken to $\mathcal{B}^{Phase}_{Ref}$, a macroscopic reference configuration essentially identical to the virgin one. However on a submacroscopic level, $\mathcal{C}^{(k)}_{R}$ reveals a multiphase structure (see Fig. 4). Averaged conformational changes occurring during the mapping from $\mathcal{B}^{(k)}_{Virg}$ to $\mathcal{B}^{Phase}_{Ref}$ are carried out by $\nabla \tilde{\mathbf{i}}^k$, which provides the average change in volume through Eq. (18). The *gray paths* indicate how positional disarrangements, switching of submicroscopic islands of LC phase, map from one configuration to the next. Sequences of classical (macroscopic) deformations $\tilde{\mathbf{y}}^{(k)}$ from either $\mathcal{B}^{Phase}_{Ref}$ essentially determine the current configuration \mathcal{B} .

size of the system and δ is of the order of 0.1 μm . Within a δ –RAE, cluster of lipids of much smaller sizes with respect to δ can coexist in different conformations (see Fig. 4 for the experimental source of this length scale).

A chart of Cartesian coordinates in any configuration, with an origin at an arbitrary material point at the headgroup-water interface, is taken. It is useful to build a link between lipid physics and continuum mechanics terminologies. We look at the virgin configuration \mathcal{B}_{Virg} of the body as the limiting case in which the vast majority of lipid clusters are in a conformational state at the interface between the gaseous and LE phases (see Fig. 1B). The LG phase here is used to define a purely homogenous liquid state of the monolayer that might exist prior to any phase transitions but with a finite surface pressure (see Fig. 1); commonly in the literature this state is referred to simply as LE however to help us differentiate between a virgin configuration that is completely homogenous and multiphase configuration we take the notational liberty of defining the LG phase. In this homogenous state, the body is practically fully relaxed and macroscopically uniform and homogeneous, conforming to the outer scale defined by FM scale space (see Fig. 4). For the physical situation at hand, this is exactly how one could conceive a virgin configuration for the monolayer. This configuration is macroscopically identical to the reference one, although by moving to the next level of monolayer scale space (see closeup 1 showing a δ -RAE at the top-left in Fig. 10) submacroscopically lipid conformations are not uniform in any δ –RAE within either reference configurations displayed in Fig. 10. Indeed, there are clusters of lipids formed by smaller subislands in the LC phase coexisting with subregions in the LE state. Our terminology labels coexistent LE-LC phases within the given δ -RAE in the reference configuration $\mathcal{B}_{Ref}^{Phase}$ as materially disarranged. This term reflects the conformational changes experienced by the lipid clusters relative to the virgin configuration. Indeed, within the given δ -RAE in $\mathcal{B}_{Ref}^{Phase}$, subislands of more packed and elongated units than the ones in the gas phase characterize the morphological variations of such lipids. Lipids in the gas phase are uniformly present throughout the virgin configuration. The more fraction of cluster of lipids within a given δ -RAE tends to include subdomains in the LC and LE phases, the more materially disarranged the body becomes within that given region. Of course between subislands in the LC and LE phases contained in the same cluster there are discontinuities in the height of the lipid tails and, hence, in the vertical component of the displacement field at the scale of such domains.

To complete the geometrical description of the system at hand, we introduce a sequence of macroscopic deformations, $\tilde{\mathbf{y}}^{(k)}$, from a reference

configuration to the current one, and its gradient $\tilde{\mathbf{F}}^{(k)}$. It is worth noting that the inverse $(\nabla \tilde{\mathbf{i}}^{(k)})^{-1}$ of the gradient of a sequence of mappings $\tilde{\mathbf{i}}^{(k)}$ (converging to the identity as the index k goes to infinity and as the size δ of the δ -RAE goes to zero) does, in fact, converge to the standard inelastic part of $\tilde{\mathbf{F}}^{(k)}$. Unlike existing methods, that can only reconstruct local infinitesimal neighborhoods of a given material particle, this convergence allows the retrieval of the whole macroscopic configuration. The latter macroscopically looks exactly the same as $\mathcal{B}^{Phase}_{ref}$ and $\mathcal{B}^{Posit}_{ref}$, with the property of being a relaxed configuration. Hence an actual entirely virgin configuration, \mathcal{B}_{Virg} , can be retrieved in this way.

We emphasize the fact that the mapping, its gradient and its inverse converge, although the the presence of the disarrangements described above implies that the sequence of the gradients $\nabla \mathbf{i}^{(k)}$ does not converge to the gradient of the limit ∇ ($\lim_{k\to+\infty}\lim_{\delta\to 0}\delta^{-2}\int_{\delta\times\delta}\mathbf{i}^{(k)}\,dA_{Virg}$) of the generating sequence $\mathbf{i}^{(k)}$. This is the case for the sequence at hand, for which $\tilde{\nabla}\mathbf{i}^{(k)}$ converges to a tensor field not equal to the identity.

To bridge the terminology between the present context and the theory of SDs we remark that, upon comparing the local blurred geometrical changes between the virgin and the reference configuration, the actual pure measure of disarrangements due to geometrical changes between the virgin and the reference configuration is the following difference

$$\nabla \left(\lim_{k \to +\infty} \lim_{\delta \to 0} \delta^{-2} \int_{\delta \times \delta} \mathbf{i}^{(k)} dA_{Virg} \right) - \lim_{k \to +\infty} \lim_{\delta \to 0} \delta^{-2} \int_{\delta \times \delta} \nabla \mathbf{i}^{(k)} dA_{Virg}.$$
(13)

It is worth noting that $\lim_{k\to +\infty} \lim_{\delta\to 0} \delta^{-2} \int_{\delta\times\delta} \mathbf{i}^{(k)} dA_{Virg}$ is the identity mapping, \mathbf{i} , which has the constant gradient \mathbf{I} , while the tensor to the left smears out the conformational changes experienced by the lipid clusters. Hence, before taking the two sets of limits above, as an approximate measure of pure conformational disarrangements the tensor field coming from the following difference can be considered:

$$\mathbf{I} - \nabla \mathbf{i}^{(k)}. \tag{14}$$

Either $\mathcal{B}_{ref}^{Phase}$ or $\mathcal{B}_{ref}^{Posit}$, once positional disarrangements have occurred, upon restricting the reasoning above to a generic δ –RAE element displayed in both configurations \mathcal{B}_{Virg} and $\mathcal{B}_{Ref}^{Phase}$, making them macroscopically identical to one another.

This tensor field represents the appropriate average of discontinuities in the vertical component of the displacement field at the scale of LC and LE subdomains, or equivalently, an average of the jumps in lipid tail heights within the small islands contained in δ –RAE.

An advantage of the approach undertaken here is that we carry on information about the geometrical changes by generating Structured Deformations (SDs) of the whole body through limiting processes, allowing us to retain key features of the determining sequence of mappings and their gradients (see Fig. 10). Such SDs come in pairs of two elements. The first element is a vector-valued field representing either the macroscopic deformation or the identity mapping. The second element is a tensor-valued field which does not need to be the gradient of the first element. This systematically accounts for the problem of geometric compatibility and applies to the configurations of the body as a whole, not just to infinitesimal neighborhoods of a given material point as it is customary in standard approaches to finite inelastic phenomena, e.g., growth in biological materials and in additive manufacturing, metal/soil/polymer finite plasticity, finite viscoelasticity, finite damage, etc.

5.1 A closer look at conformational changes

Within a subdomain of the reference configuration $\mathcal{B}_{Ref}^{Phase}$ termed δ –RAE, a microstructure exists which experiments confirm is a coexistence of nanoislands of LC and LE phases (see Figs. 4 and 10). Comparing δ – RAE $\in \mathcal{B}_{Ref}^{Phase}$ to δ – RAE $\in \mathcal{B}_{Virg}$, it is clear lipid conformational changes have occurred. The change in lipid tail height compared to the fully relaxed configuration \mathcal{B}_{Virg} can be taken as purely morphological since any energy stored in the tails is negligible compared to the headgroups. Nevertheless, as seen in Fig. 10, evaluating an averaged measure $\lambda_3^{(k,\delta)}$ of lipid tail elongations is key to understanding monolayer mechanics. By defining $\lambda_{LC}^{(k,\delta)} = h_{(R)}^{(k)}$ L_C $h_{Virg}^{(k)}$, $c_{LC}^{(k,\delta)} = dA_{LC}^{(k,\delta)}/dA_{Ref}$ and $\lambda_{LE}^{(k,\delta)} = h_{(R)}^{(k)}$ L_C $h_{Virg}^{(k)}$, $c_{LE}^{(k,\delta)} = dA_{LC}^{(k,\delta)}$ as the changes in elongation and area concentrations of lipid clusters in the LC and the LE phases, respectively, one can calculate the average elongation of lipid tails within a subdomain of the monolayer

^b As δ goes to zero and k tends to infinity.

$$\lambda_{3}^{(k,\delta)} = \frac{c_{LC}^{(k,\delta)} \lambda_{LC}^{(k,\delta)^{2}} + c_{LE}^{(k,\delta)} \lambda_{LE}^{(k,\delta)^{2}}}{c_{LC}^{(k,\delta)} \lambda_{LC}^{(k,\delta)} + c_{LE}^{(k,\delta)} \lambda_{LE}^{(k,\delta)}}.$$
(15)

 $\lambda_{LC}^{(k,\delta)}$ and $\lambda_{LE}^{(k,\delta)}$ within each subcluster of a given δ –RAE of the reference configuration $\mathcal{B}_{Ref}^{Phase}$ are considered constant. This is justified since physically these are two different thermodynamic phases, connected by a first-order phase transition. The respective surface concentrations of the two phases, $c_{LC}^{(k,\delta)}$ and $c_{LE}^{(k,\delta)}$, however, can change from point to point in-plane even within a given δ –RAE of the reference configuration.

Recall that the identity tensor \mathbb{P} for in-plane transformations is simply the projector of tensors onto the reference plane of the monolayer, namely

$$\mathbb{P} = \mathbf{I} - \mathbf{E}_3 \otimes \mathbf{E}_3. \tag{16}$$

Furthermore, we recall that the measured area changes between the reference and virgin configurations is the second invariant of the projection of the material gradient $\mathbb{P} \tilde{\nabla} \mathbf{i}^{(k)}$ onto the reference plane for the body, namely

$$dA_{Ref}/dA_{Virg} = det(\mathbb{P}\,\tilde{\nabla}\mathbf{i}^{(k)}) \tag{17}$$

Henceforth, upon factoring this term across both the numerator and the denominator of Eq. (15), we can easily refer to the area concentration of the LC and LE phases relative to the virgin configuration.

Local volume changes of lipid clusters during conformational changes have to be computed to account for the second aspect of tail morphological variations, namely their projection onto the headgroup-water interface. The local averaged volume change can be written as

$$det(\tilde{\nabla}\mathbf{i}^{(k)}) = \lambda_3^{(k,\delta)} det(\mathbb{P}\,\tilde{\nabla}\mathbf{i}^{(k)}) \tag{18}$$

This same result is obtained by comparing the local volume measures within $\mathcal{B}_{Ref}^{Phase}$ and \mathcal{B}_{Virg} . To derive this, we first define the averaged heights $h_{Ref}^{(k,\delta)}$ and $h_{Virg}^{(k,\delta)}$ as the heights of the lipid clusters within $\mathcal{B}_{Ref}^{Phase}$ and \mathcal{B}_{Virg} , respectively; and, as mentioned above, $h_{(R)\ LC}^{(k,\delta)}$ and $h_{(R)\ LE}^{(k,\delta)}$ the actual heights of lipid clusters within \mathcal{C}_{R}^{k} (see Fig. 10). The volume occupied by the clusters at a point

Evidently, while dA_{Ref} denotes the area measure of an infinitesimal surface patch within a given δ -RAE in the reference configuration, the quantities $dA_{LC}^{(k,\delta)}$ and $dA_{LC}^{(k,\delta)}$ indicate the corresponding local area measures of the lipid clusters within the LC and the LE phase in that same configuration.

inside δ -RAE $\in \mathcal{B}^{Phase}_{Ref}$ can then be written as follows: $h^{(k,\delta)}_{Ref} dA_{Ref} = h^{(k,\delta)}_{(R)\ LC} dA^{(k,\delta)}_{(R)\ LC} + h^{(k,\delta)}_{(R)\ LE} dA^{(k,\delta)}_{(R)\ LE}$. We map this relationship into \mathcal{B}_{Virg} by dividing both sides by $h^{(k,\delta)}_{Virg}$ followed by dividing and multiplying each area measure by dA_{Virg} to obtain:

$$c_{LC}^{(k,\delta) \ Virg} \lambda_{LC}^{(k,\delta)} + c_{LE}^{(k,\delta) \ Virg} \lambda_{LE}^{(k,\delta)} = \lambda_3^{(k,\delta)} \det(\mathbb{P} \ \tilde{\nabla} \mathbf{i}^{(k)})$$
(19)

where $\lambda_3^{(k,\delta)} = h_{Ref}^{(k,\delta)}/h_{Virg}^{(k,\delta)}$, $c_{LC}^{(k,\delta)\ Virg} = c_{LC}^{(k,\delta)}\ det(\mathbb{P}\ \tilde{\nabla}\mathbf{i}^{(k)})$ and $c_{LE}^{(k,\delta)\ Virg} = c_{LE}^{(k,\delta)}\ det(\mathbb{P}\ \tilde{\nabla}\mathbf{i}^{(k)})$ are the surface concentrations relative to the virgin configurations of LC and LE phases, respectively. On the other hand, local volume conservation requires that $h_{Ref}^{(k,\delta)}\ dA_{Ref} = h_{Virg}^{(k,\delta)}\ dA_{Virg}\ det(\tilde{\nabla}\mathbf{i}^{(k)})$, hence Eq. (18) and

$$det(\tilde{\nabla}\mathbf{i}^{(k)}) = c_{LC}^{(k,\delta) \ Virg} \lambda_{LC}^{(k,\delta)} + c_{LE}^{(k,\delta) \ Virg} \lambda_{LE}^{(k,\delta)}$$
(20)

follow. The right hand side of the last relationship can be reinterpreted upon considering the restrictions of the sequence $\tilde{\mathbf{i}}^{(k)}$, $\tilde{\mathbf{i}}^{(k)}_{LC}$, and $\tilde{\mathbf{i}}^{(k)}_{LE}$, to the counter-images of the domains in the LC and LE phases. For such mappings, Eq. (20) reads as follows $det(\tilde{\nabla}\mathbf{i}^{(k)}) = det(\tilde{\nabla}\mathbf{i}^{(k)}_{LC}) + det(\tilde{\nabla}\mathbf{i}^{(k)}_{LE})$. In turn, Eq. (20) expresses the fact that volume concentrations relative to the reference configuration, $c^{(k,\delta)}_{Vol\ LC} = dV^{(k,\delta)}_{LC}/dV_{Ref} = (det(\tilde{\nabla}\mathbf{i}^{(k)}))^{-1}\ det(\tilde{\nabla}\mathbf{i}^{(k)}_{LC})$, $c^{(k,\delta)}_{Vol\ LE} = dV^{(k,\delta)}_{LE}/dV_{Ref} = (det(\tilde{\nabla}\mathbf{i}^{(k)}))^{-1}\ det(\tilde{\nabla}\mathbf{i}^{(k)}_{LC})$, of the LC and LE phases form the totality of lipid population, namely $c^{(k,\delta)}_{Vol\ LC} + c^{(k,\delta)}_{Vol\ LE} = 1$. We can now revisit Eq. (15). In particular, by substituting Eq. (18) into (20), we obtain

$$\lambda_3^{(k,\delta)} = c_{Vol\ LC}^{(k,\delta)} \ \lambda_{LC}^{(k,\delta)} + c_{Vol\ LE}^{(k,\delta)} \ \lambda_{LE}^{(k,\delta)}$$
 (21)

which gives a more revealing measurement of the average elongation of lipid tails within a subdomain of the monolayer as it moves between \mathcal{B}_{Virg} and $\mathcal{B}_{Ref}^{Phase}$. By taking the average of $\lambda_3^{(k,\delta)}$ over an area element δ^2 defined by δ –RAE $\in \mathcal{B}_{Ref}^{Phase}$ a mean value of this field within such an element can be obtained: $\langle \lambda_3^{(k,\delta)} \rangle = \delta^{-2} \int_{\delta \times \delta} \lambda_3^{(k,\delta)} \, dA_{Ref}$. Given that $\lambda_{LC}^{(k,\delta)}$ and $\lambda_{LC}^{(k,\delta)}$ are constant throughout the given δ –RAE, we obtain

$$\langle \lambda_3^{(k,\delta)} \rangle = \langle c_{Vol\ LC}^{(k,\delta)} \rangle \ \lambda_{LC}^{(k,\delta)} + \langle c_{Vol\ LE}^{(k,\delta)} \rangle \ \lambda_{LE}^{(k,\delta)}. \tag{22}$$

Henceforth, notationally $\lambda_3^{(k)}$ will refer to $\langle \lambda_3^{(k,\delta)} \rangle$.

We are now in a position to characterize $\mathbf{I} - \nabla \mathbf{i}^{(k)}$, the measure of pure conformational disarrangements. The sequence of gradients of identity mappings describing the conformational changes of the lipid clusters at hand reads as follows:

$$\tilde{\nabla \mathbf{i}}^{(k)} = \left(\det\left(\mathbb{P}\tilde{\nabla \mathbf{i}}^{(k)}\right)\right)^{1/2} \quad \frac{\circ}{\mathbb{P}\tilde{\nabla \mathbf{i}}^{(k)}} + \lambda_3^{(k)} \, \mathbf{E}_3 \otimes \mathbf{E}_3 \tag{23}$$

where $\overline{\mathbb{P}\tilde{\nabla}\mathbf{i}^{(k)}} = \left(\det\left(\mathbb{P}\;\tilde{\nabla}\;\mathbf{i}^{(k)}\right)\right)^{-1/2}\;\mathbb{P}\tilde{\nabla}\mathbf{i}^{(k)}$ is the area preserving (in-plane isochoric part) of the restriction of the disarrangement tensor to the midplane. The measure of pure conformational disarrangements then becomes:

$$\mathbf{I} - \tilde{\nabla} \mathbf{i}^{(k)} = \mathbb{P} - \left(\det \left(\mathbb{P} \tilde{\nabla} \mathbf{i}^{(k)} \right) \right)^{1/2} \quad \frac{\circ}{\mathbb{P} \tilde{\nabla} \mathbf{i}^{(k)}} + \left(1 - \lambda_3^{(k)} \right) \mathbf{E}_3 \otimes \mathbf{E}_3 \tag{24}$$

Of note, the average measures of pure in-plane and out-of-plane disarrange-

ments are given by
$$\mathbb{P} - \left(\det\left(\mathbb{P}\tilde{\nabla}\mathbf{i}^{(k)}\right)\right)^{1/2} \stackrel{\circ}{\mathbb{P}\tilde{\nabla}\mathbf{i}^{(k)}}$$
 and $1 - \lambda_3^{(k)}$, respectively.

In order to retain only in-plane features of the conformational changes contributing to the local average monolayer compressibility and its spatial gradients, we uncouple the direct influence of the out-of-plane morphological variations of the lipid tails within clusters in the given δ –RAE through the following factorization of the tensor $\tilde{\nabla}\mathbf{i}^{(k)}$:

$$\tilde{\nabla \mathbf{i}}^{(k)} = \left((\lambda_3^{(k)} \det(\mathbb{P}\tilde{\nabla} \mathbf{i}^{(k)}))^{1/2} \right)^{1/2} = \mathbb{P}\tilde{\nabla \mathbf{i}}^{(k)} + \mathbf{E}_3 \otimes \mathbf{E}_3 \left(\lambda_3^{(k)} \right)^{-1/2} \mathbb{P} + \lambda_3^{(k)} \mathbf{E}_3 \otimes \mathbf{E}_3$$
(25)

The tensor appearing to the right of this multiplicative decomposition of $\nabla \tilde{i}^{(k)}$ incorporates:

• the average change in volume $det(\tilde{\nabla}\mathbf{i}^{(k)}) = \lambda_3^{(k)} det(\mathbb{P}\tilde{\nabla}\mathbf{i}^{(k)})$, labeled in Eq. (18), due to conformational changes from \mathcal{B}_{Virg} to $\mathcal{B}_{Ref}^{Phase}$;

• geometrical area preserving (averaged measure of) in-plane morphological variations $\mathbb{P}\tilde{\nabla}\mathbf{i}^{(k)}$, which would simply become \mathbb{P} if no such redistributions occurred.

and at the same time the factorized form allows for uncoupling the direct influence of the out-of-plane conformational changes of the lipid tails within clusters in δ –RAE (such an influence remains confined to the right factor of Eq. 25).

Since purely elongational changes within lipid tails do not contribute to monolayer energy storage, it is physically reasonable to assume that the monolayer energy density (not defined in this manuscript) is a function of lipid morphological variations represented through $\mathbf{K}^{(k)}$ alone. Eq. (25) allows us to identify this variable as

$$\mathbf{K}^{(k)} = (\lambda_3^{(k)} \det(\mathbb{P} \nabla \mathbf{i}^{(k)}))^{1/2} \quad \overline{\mathbb{P} \tilde{\nabla} \mathbf{i}^{(k)}}$$
 (26)

5.2 Macroscopic deformation

The overall deformation of the body is envisioned as a sequence of macroscopic (vector-valued) fields

$$\tilde{\mathbf{y}}^{(k)} = \mathbf{y}^{(k)} + \tilde{\boldsymbol{\phi}}_3^{(k)} X_3 \mathbf{E}_3,$$
 (27)

where k simply labels the order of such a sequence, $\mathbf{y}^{(k)} = y_{\alpha}^{(k)} \mathbf{e}_{\alpha}$, $\alpha = 1, 2$, depends only on the in-plane coordinates (not on X_3), and so does $\tilde{\phi}_3^{(k)} = h^{(k,\delta)}/h_{Ref}^{(k,\delta)}$, where $h^{(k,\delta)}$ is the average measure of the tail thickness at a location in space situated within the image in the current configuration (see Fig. 10 to the bottom right) of a given δ –RAE mapped from the reference configuration (either $\mathcal{B}_{Ref}^{Phase}$ or $\mathcal{B}_{Ref}^{Posit}$). In other words $\tilde{\phi}_3^{(k)}$ is an averaged macroscopic measure of the tail's length change at a given location \mathbf{x} within the current configuration relative to the corresponding material particle $\mathbf{X} = \mathbf{y}^{(k)-1}(\mathbf{x})$, where $\mathbf{y}^{(k)-1}$ simply denotes the inverse of the macroscopic deformation at hand.

^d Of course the restriction to the plane of the monolayer of the sequence of macroscopic deformation gradients will play a key role in the energy as well, as it will have to combine with \mathbf{K}^k to deliver the appropriate geometric measure of geometrical changes upon which energy is stored.

Here $\{\mathbf{e}_{\alpha}\}_{\{\alpha=1,\ 2\}}$ is an orthonormal basis taken at the water-headgroup interface in the current configuration, while the unit vector in the third direction remains the same as before deformation. The overall geometric changes of the water-headgroup layer are then described by restricting the sequence of macroscopic deformations (Eq. 27) to points located in the reference plane at $X_3=0$. Henceforth, by restricting the out-of-plane component of the macroscopic deformation to have spatially slow variations in-plane within a given δ –RAE (for instance piecewise constant in plane within the given δ –RAE), then $\tilde{\phi}_{3,\alpha}^{(k)}\approx 0$, and the approximate form for the gradient of $\tilde{\mathbf{y}}^{(k)}$ becomes

$$\tilde{\mathbf{F}}^{(k)} = \mathbf{F}^{(k)} + \tilde{\boldsymbol{\phi}}_{3}^{(k)} \quad \mathbf{E}_{3} \otimes \mathbf{E}_{3}, \tag{28}$$

which is exact at the water-headgroup interface, i.e., at $X_3=0$. This sequence of gradients describes the local features (blurred out within the given δ –RAE) of the macroscopic geometrical changes. We note that $\mathbf{F}^{(k)}=\mathbf{y}_{,A}^{(k)}\otimes\mathbf{E}_A$ (as usual, repeated indexes means sum among the items with the same index) gives information about the in-plane macroscopic variations of the geometry of the monolayer with respect to changes in position in a reference configuration \mathcal{B}_{Ref} (either $\mathcal{B}_{Ref}^{Phase}$ or $\mathcal{B}_{Ref}^{Posit}$ to be discussed later). Here the notation $\circ_{,A}=\frac{\partial \circ}{\partial X_A}$, with A=1,2, and where $X\equiv (X_1,X_2)$ denotes both a generic in-plane material particle in \mathcal{B}_{Ref} and the in-plane coordinate chart in the same configuration. Of note, we bear in mind that the sequence of macroscopic deformation gradients does account for both geometrical changes due to and without disarrangements. $^{\circ}$

5.3 A measure of geometrical changes without disarrangements

It is key to recall that elongational changes of the tails are only conformational, hence no energy can be stored through the morphological variations of the lipid tails. A strictly kinematic, and somewhat related issue, is how material elements taken within any δ –RAE in the virgin configuration

^e For future references it is useful to keep track of the restriction of the gradient of the macroscopic deformation to any horizontal plane (e.g., the lipid-water interface). This has been already introduced in the text in Eq. (16). Considerations about the isochoricity are obsolete: we must get rid of them. In particular, we note that $\mathbf{y}_{\mathcal{A}}^{(k)} \otimes \mathbf{E}_{\mathcal{A}} = F_{a_{\mathcal{A}}}^{(k)}$ and $\mathbf{E}_{\mathcal{A}} \otimes \mathbf{E}_{\mathcal{A}}$, after setting $F_{a_{\mathcal{A}}}^{(k)} = \mathbf{y}_{a_{\mathcal{A}}}^{(k)}$.

deform without any kind of disarrangements caused by jumps, voids, switching, etc. Fig. 10 and the basis of the theory of SDs help to state that this local transformation is given by the mutiplicative decomposition $\tilde{\mathbf{G}}^{(k)} = \tilde{\mathbf{F}}^{(k)} \tilde{\nabla} \mathbf{i}^{(k)}$ between the macroscopic deformation gradient, denoted by $\tilde{\mathbf{F}}^{(k)}$, and the tensor $\nabla \tilde{i}^{(k)}$. This is consistent with the fact that, upon taking the material gradient (relative to changes of the material particle in \mathcal{B}_{Virg}) of the composition of mappings $\tilde{\mathbf{y}}^{(k)} \circ \tilde{\mathbf{i}}^{(k)}$ (transforming each material particle \mathbf{X} in the virgin configuration onto its corresponding location $\mathbf{x} = (\tilde{\mathbf{y}}^{(k)} \circ \tilde{\mathbf{i}}^{(k)})(\mathbf{X})$ in the current one) the result is still that same multiplicative decomposition for $\tilde{\mathbf{G}}^{(k)}$ just mentioned above.

This composition relates with the "elastic part" of the macroscopic deformation gradient in standard treatments of bodies undergoing finite deformations and nonelastic phenomena such as growth, remodeling, plasticity, etc., as $\tilde{\mathbf{F}}^{(k)} = \tilde{\mathbf{G}}^{(k)} \left(\tilde{\nabla} i^{(k)} \right)^{-1}$. In spite of this striking analogy, SDs do not require giving constitutive attributes to the purely geometrical entities $\tilde{\mathbf{F}}^{(k)}$, $\tilde{\mathbf{G}}^{(k)}$, and $\tilde{\nabla} i^{(k)}$ involved in the decompositions above. Finally, based on Eqs. (23), (26), and (28) an approximate measure of deformation without disarrangements (which holds in this exact form at the waterheadgroup interface and layer) $\tilde{\mathbf{G}}^{(k)}$ takes the following form:

$$\tilde{\mathbf{G}}^{(k)} = \mathbf{G}^{(k)} + \lambda_3^{(k)} \tilde{\boldsymbol{\phi}}_3^{(k)} \mathbf{E}_3 \otimes \mathbf{E}_3, \tag{29}$$

where

$$\mathbf{G}^{(k)} = \mathbb{P} \,\tilde{\mathbf{G}}^{(k)} = \mathbf{F}^{(k)} \mathbf{K}^{(k)}. \tag{30}$$

This latter tensor field is the geometrical variable directly determining the energy density of the monolayer. This explains how the local averaged measure of conformational changes $\mathbf{K}^{(k)}$ and the corresponding part $\mathbf{F}^{(k)}$ of the deformation gradient combine to deliver the appropriate geometric variable upon which the stored energy density of the monolayer depends. It is worth noting that (26) allows us to look into the structure of $\mathbf{G}^{(k)}$ and note that $\lambda_3^{(k)}$ directly enters into such a variable. Furthermore, if a particular situation in

In Fig. 10, the composition between $\tilde{\mathbf{F}}^{(k)}$ and $\tilde{\nabla}_{\mathbf{I}}^{(k)}$ represents what happens locally to any material element in an infinitesimal neighborhood of a particle inside any δ –RAE in the virgin configuration after deformation from \mathcal{B}_{Virg} to the current configuration \mathcal{B} .

which conformational changes are uniform in-plane (i.e., in-plane "hydrostatic"), i.e., $\mathbb{P}\tilde{\nabla} i^{(k)} = \mathbb{P}$, then $\mathbf{G}^{(k)} = (\lambda_3^{(k)} \det \mathbb{P} \nabla i^{(k)})^{1/2} \mathbf{F}^{(k)}$.

5.4 Positional disarrangements

Positional disarrangements may arise within planar subregions of the monolayer bearing trace at the water-headgroup interface and inside the layer in the immediate proximity of the interface. This can happen during material instabilities, such as shear bands: banding regions are, in fact, extensively reported in the first part of this work. Positional disarrangements, visualized in Fig. 10 within the closeup 2 and displayed to the top right of the figure inside δ –RAE in \mathcal{B}_{Ref}^{Pos} , may involve switching of subclusters of lipids once locally a certain stress-strain state is reached. The envisioned physical mechanism is analogous to granular materials experiencing shear bands (Tordesillas et al., 2011, 2016). The idea is that under a significantly dominant compressive state of stress, at a critical level of such loading, during deformation, subclusters in the LC phase and the ones in the LE displayed in δ -RAE in the reference configuration $\mathcal{B}^{\textit{Phase}}_{\textit{Ref}}$ would disarrange almost like grains jamming and, hence, by switching positions with other clusters, lead to banding as seen in Fig. 10 and seen experimentally with lipid monolayers in the generalized collapse phase diagram presented in Fig. 2.

6. Conclusions

Lipid monolayers provide a rich system in which to explore and study the mechanics of thin self-assembled films with unparalleled details. The importance of lipid films in technological and biological applications and systems is unquestioned. Lipid monolayers such as lung surfactants or cell membranes composed of lipid bilayers are often exposed to mechanical forces that lead to mechanical instabilities, which in turn impact the large-scale behavior of the system. We provide the first step toward a unified general theory of lipid film continuum mechanics. We show that in monolayers, irrespective of composition, five canonical collapse modes can be accessed. Furthermore, the different modes of collapse can be tuned through composition in multicomponent systems or simply temperature in single-component monolayers. Furthermore, lipid monolayers can be probed on multiple microscopy length scales, building a rich multidimensional image data space. We provide a scale space to unify these different lengths

and allow for a common language in which to build the topology of lipid monolayer structure. In the section on multiscale geometry, we provide a formal analytical description of this topology for lipid monolayers that undergo banding. The geometric kinematics developed in this paper are the first step to a generalized mechanical model of lipids. In future work, these kinematics will be used in the context of structured deformation theory to build constitutive models of lipids intrinsically grounded in their multiscale structure. These continuum models will then be validated and tested using finite element analysis, a methodology successfully applied to lipid monolayers in the present paper.

Acknowledgments

A.R.C., M.F., and L.D. acknowledge the support of the Italian Ministry of Education, University and Research (MIUR) through the grant PRIN-20177TTP3S. A.R.C., M.F., and L.D. also acknowledge the support of the MIUR through the grant PON-ARS01-01384. L.D. is also supported by the European Commission H2020 FET Proactive "Neurofibres" grant no. 732344 as well as by the MIUR under the "Departments of Excellence" grant L.232/2016, and by the FET Open "Boheme" grant no. 863179. A.R.C. acknowledges the support of the grant PON-AIM1849854-1. L.P., K.C., and N.N. acknowledge the support of the National Institutes of Health, National Heart, Lung, and Blood Institute grant 1R01HL159205-01.

References

- Andelman, D., Brochard, F., Knobler, C., & Rondelez, F. (1994). Structures and phase transitions in Langmuir monolayers. In W. M. Gelbart, A. Ben-Shaul, & D. Roux (Eds.), *Micelles, membranes, microemulsions, and monolayers* (pp. 559–602). New York, NY: Springer New York. https://doi.org/10.1007/978-1-4613-8389-5 (Eds.).
- Boal, D. (2002). Mechanics of the cell. Cambridge, UK: Cambridge University Press.
- Boatwright, T., Levine, A. J., & Dennin, M. (2010). Tracking giant folds in a monolayer. *Langmuir*, 26(15), 12755–12760. https://doi.org/10.1021/la1012439.
- Callens, M., Beltrami, M., D'Agostino, E., Pfeiffer, H., Verellen, D., Paradossi, G., & Van Den Abeele, K. (2019). The photopolymerization of DC8,9PC in microbubbles. Colloids and Surfaces A: Physicochemical and Engineering Aspects, 568, 371–380. https://doi.org/10.1016/j.colsurfa.2019.01.038.
- Carotenuto, A. R., Lunghi, L., Piccolo, V., Babaei, M., Dayal, K., Pugno, N., ... Fraldi, M. (2020). Mechanobiology predicts raft formations triggered by ligand-receptor activity across the cell membrane. *Journal of the Mechanics and Physics of Solids*, 141, 103974. https://doi.org/10.1016/j.jmps.2020.103974.
- Chua, Y., Leahy, B., Zhang, M., You, S., Lee, K. Y. C., Coppersmith, S. N., & Lin, B. (2013). Incommensurate phases of a supported nanoparticle film subjected to uni-axial compression. *Proceedings of the National Academy of Sciences*, 110(3), 824–831. https://doi.org/10.1073/pnas.1101630108.
- Cicuta, P., & Vella, D. (2009). Granular character of particle rafts. *Physical Review Letters*, 102(13), 138302. https://doi.org/10.1103/PhysRevLett.102.138302.
- Dassault Systèmes. (2018). Dassault Systèmes.

- Deseri, L., & Owen, D. R. (2003). *Journal of Elasticity*, 70(1), 197–236. https://doi.org/10.1023/B:ELAS.0000005584.22658.b3.
- Deseri, L., & Owen, D. R. (2013). Moving interfaces that separate loose and compact phases of elastic aggregates: A mechanism for drastic reduction or increase in macroscopic deformation. *Continuum Mechanics and Thermodynamics*, 25(2–4), 311–341. https://doi.org/10.1007/s00161-012-0260-y.
- Deseri, L., & Owen, D. R. (2019). *Journal of Elasticity*, 135(1–2), 149–182. https://doi.org/10.1007/s10659-018-9707-0.
- Diamant, H., Witten, T. A., Ege, C., Gopal, A., & Lee, K. Y. C. (2001). Topography and instability of monolayers near domain boundaries. *Physical Review E*, 63(6), 061602. https://doi.org/10.1103/PhysRevE.63.061602.
- Diamant, H., Witten, T. A., Gopal, A., & Lee, K. Y. C. (2000). Unstable topography of biphasic surfactant monolayers. *Europhysics Letters (EPL)*, 52(2), 171–177. https://doi.org/10.1209/epl/i2000-00419-1.
- Fennell Evans, D., & Wennerström, H. (1999). The colloidal domain: Where physics, chemistry, biology, and technology meet. New York: Wiley-VCH.
- Fields, C. G., Lloyd, D. H., Macdonald, R. L., Otteson, K. M., & Noble, R. L. (1991). HBTU activation for automated Fmoc solid-phase peptide synthesis. *Peptide Research*, 4(2), 95–101.
- Fung, Y. C. (1993). Biomechanics—Mechanical properties of living tissues. New York: Springer-Verlag.
- Garg, S., Thomas, A. A., & Borden, M. A. (2013). The effect of lipid monolayer in-plane rigidity on in vivo microbubble circulation persistence. *Biomaterials*, 34(28), 6862–6870. https://doi.org/10.1016/j.biomaterials.2013.05.053.
- Gopal, A., Belyi, V. A., Diamant, H., Witten, T. A., & Lee, K. Y. C. (2006). Microscopic folds and macroscopic jerks in compressed lipid monolayers. *The Journal of Physical Chemistry B*, 110(21), 10220–10223. https://doi.org/10.1021/jp0618983.
- Gopal, A., & Lee, K. Y. C. (2001). Morphology and collapse transitions in binary phospholipid monolayers. *The Journal of Physical Chemistry B*, 105(42), 10348–10354. https://doi.org/10.1021/jp012532n.
- Goto, T. E., & Caseli, L. (2013). Understanding the collapse mechanism in langmuir monolayers through polarization modulation-infrared reflection absorption spectroscopy. *Langmuir*, 29(29), 9063–9071. https://doi.org/10.1021/la402044c.
- Holten-Andersen, N., Henderson, J. M., Walther, F. J., Waring, A. J., Ruchala, P., Notter, R. H., & Lee, K. Y. C. (2011). KL4 peptide induces reversible collapse structures on multiple length scales in model lung surfactant. *Biophysical Journal*, 101(12), 2957–2965. https://doi.org/10.1016/j.bpj.2011.10.050.
- Hunt, G. W., Tordesillas, A., Green, S. C., & Shi, J. (2010). Force-chain buckling in granular media: A structural mechanics perspective. *Philosophical Transactions of the Royal Society A: Mathematical, Physical and Engineering Sciences*, 368(1910), 249–262. https://doi.org/10. 1098/rsta.2009.0180.
- Junghans, A., Waltman, M. J., Smith, H. L., Pocivavsek, L., Zebda, N., Birukov, K., ... Majewski, J. (2014). Understanding dynamic changes in live cell Adhesion with neutron reflectometry. *Modern Physics Letters*. B, 28(30), 14300154. https://doi.org/10.1142/ S0217984914300154.
- Junghans, A., Watkins, E. B., Barker, R. D., Singh, S., Waltman, M. J., Smith, H. L., ... Majewski, J. (2015). Analysis of biosurfaces by neutron reflectometry: From simple to complex interfaces. *Biointerphases*, 10(1), 019014. https://doi.org/10.1116/1.4914948.
- Kaganer, V. M., Möhwald, H., & Dutta, P. (1999). Structure and phase transitions in lang-muir monolayers. Reviews of Modern Physics, 71(3), 779–819. https://doi.org/10.1103/RevModPhys.71.779.

- Kim, K., Choi, S. Q., Zell, Z. A., Squires, T. M., & Zasadzinski, J. A. (2013). Effect of cholesterol nanodomains on monolayer morphology and dynamics. *Proceedings of the National Academy of Sciences*, 110(33), E3054–E3060. https://doi.org/10.1073/pnas.1303304110.
- Kwan, J. J., & Borden, M. A. (2012a). Lipid monolayer collapse and microbubble stability. Advances in Colloid and Interface Science, 183–184, 82–99. https://doi.org/10.1016/j.cis. 2012.08.005.
- Kwan, J. J., & Borden, M. A. (2012b). Lipid monolayer dilatational mechanics during microbubble gas exchange. Soft Matter, 8, 4756–4766. https://doi.org/10.1039/ C2SM07437K.
- Leahy, B. D., Pocivavsek, L., Meron, M., Lam, K. L., Salas, D., Viccaro, P. J., ... Lin, B. (2010). Geometric stability and elastic response of a supported nanoparticle film. *Physical Review Letters*, 105(5), 058301. https://doi.org/10.1103/PhysRevLett.105. 058301.
- Lee, K. Y. C., Lipp, M. M., Takamoto, D. Y., Ter-Ovanesyan, E., Zasadzinski, J. A., & Waring, A. J. (1998). Apparatus for the continuous monitoring of surface morphology via Fluorescence microscopy during monolayer transfer to substrates. *Langmuir*, 14(9), 2567–2572. https://doi.org/10.1021/la9704213.
- Lin, B., Schultz, D. G., Lin, X.-M., Li, D., Gebhardt, J., Meron, M., & Viccaro, P. J. (2007). Langmuir monolayers of gold nanoparticles. *Thin Solid Films*, 515(14), 5669–5673. https://doi.org/10.1016/j.tsf.2006.12.023.
- Lipp, M. M., Lee, K. Y. C., Takamoto, D. Y., Zasadzinski, J. A., & Waring, A. J. (1998). Coexistence of buckled and flat monolayers. *Physical Review Letters*, 81(8), 1650–1653. https://doi.org/10.1103/PhysRevLett.81.1650.
- Liu, Q., Sun, Z., & Santamarina, J. C. (2021). Self-assembled nanoparticle-coated interfaces: Capillary pressure, shell formation and buckling. *Journal of Colloid and Interface Science*, 581, 251–261. https://doi.org/10.1016/j.jcis.2020.07.110.
- Lu, W., Knobler, C. M., Bruinsma, R. F., Twardos, M., & Dennin, M. (2002). Folding Langmuir monolayers. *Physical Review Letters*, 89(14), 146107. https://doi.org/10. 1103/PhysRevLett.89.146107.
- Majumdar, S., Krishnaswamy, R., & Sood, A. K. (2011). Shear banding in a yield stress bearing Langmuir monolayer. *Soft Matter*, 7(17), 7805–7812. https://doi.org/10.1039/C1SM05462G.
- Majumdar, S., & Sood, A. K. (2008). Nonequilibrium fluctuation relation for sheared micellar gel in a jammed state. *Physical Review Letters*, 101(7), 078301. https://doi.org/10.1103/PhysRevLett.101.078301.
- McConnell, H. M. (1991). Structures and transitions in lipid monolayers at the air-water interface. *Annual Review of Physical Chemistry*, 42(1), 171–195. https://doi.org/10.1146/annurev.pc.42.100191.001131.
- Möhwald, H. (1990). Phospholipid and phospholipid-protein monolayers at the air/water interface. *Annual Review of Physical Chemistry*, 41(1), 441–476. https://doi.org/10.1146/annurev.pc.41.100190.002301.
- Möhwald, H. (1993). Surfactant layers at water surfaces. *Reports on Progress in Physics*, *56*(5), 653–685. https://doi.org/10.1088/0034-4885/56/5/002.
- Nguyen, N., & Waas, A. M. (2016). Nonlinear, finite deformation, finite element analysis. Zeitschrift für Angewandte Mathematik und Physik, 67(3), 35. https://doi.org/10.1007/s00033-016-0623-5.
- Nikomarov, E. S. (1990). A slow collapse of a monolayer spread on an aqueous surface. Langmuir, 6(2), 410–414. https://doi.org/10.1021/la00092a021.
- Oppenheimer, N., Diamant, H., & Witten, T. A. (2013). Anomalously fast kinetics of lipid monolayer buckling. *Physical Review E*, 88(2), 022405. https://doi.org/10.1103/PhysRevE.88.022405.

- Piknova, B., Schram, V., & Hall, S. B. (2002). Pulmonary surfactant: Phase behavior and function. *Current Opinion in Structural Biology*, 12(4), 487–494. https://doi.org/10.1016/s0959-440x(02)00352-4.
- Pocivavsek, L., Dellsy, R., Kern, A., Johnson, S., Lin, B., Lee, K. Y. C., & Cerda, E. (2008). Stress and fold localization in thin elastic membranes. *Science*, 320(5878), 912–916. https://doi.org/10.1126/science.1154069.
- Pocivavsek, L., Frey, S. L., Krishan, K., Gavrilov, K., Ruchala, P., Waring, A. J., ... Lee, K. Y. C. (2008). Lateral stress relaxation and collapse in lipid monolayers. *Soft matter*, 4, 2019–2029. https://doi.org/10.1039/b804611e.
- Pocivavsek, L., Gavrilov, K., Cao, K. D., Chi, E. Y., Li, D., Lin, B., ... Lee, K. Y. C. (2011). Glycerol-induced membrane stiffening: The role of viscous fluid adlayers. *Biophysical Journal*, 101(1), 118–127. https://doi.org/10.1016/j.bpj.2011.05.036.
- Pocivavsek, L., Junghans, A., Zebda, N., Birukov, K., & Majewski, J. (2013). Tuning endothelial monolayer adhesion: A neutron reflectivity study. *American Journal of Physiology-Lung Cellular and Molecular Physiology*, 306(1), L1–L9. https://doi.org/10.1152/ajplung.00160.2013.
- Pocivavsek, L., Leahy, B., Holten-Andersen, N., Lin, B., Lee, K. Y. C., & Cerda, E. (2009). Geometric tools for complex interfaces: From lung surfactant to the mussel byssus. *Soft Matter*, 5(10), 1963. https://doi.org/10.1039/b817513f.
- Ries, H. E. (1979). Stable ridges in a collapsing monolayer. *Nature*, 281(5729), 287–289. https://doi.org/10.1038/281287a0.
- Robertson, B., & Halliday, H. L. (1998). Principles of surfactant replacement. *Biochimica Et Biophysica Acta*, 1408(2–3), 346–361. https://doi.org/10.1016/s0925-4439(98)00080-5.
- Safran, S. (1994). Statistical thermodynamics of surfaces, interfaces and membranes. Reading, MA: Addison-Wesley.
- Saint-Jalmes, A., Assenheimer, M., & Gallet, F. (1998). Surface tension and compression modulus anisotropies of a phospholipid monolayer spread on water and on formamide. *The Journal of Physical Chemistry B*, 102(30), 5810–5815. https://doi.org/10.1021/jp980541z.
- Saint-Jalmes, A., & Gallet, F. (1998). Buckling in a solid Langmuir monolayer: Light scattering measurements and elastic model. *The European Physical Journal B*, 2, 489–494. https://doi.org/10.1007/s100510050272.
- Saint-Jalmes, A., Graner, F., Gallet, F., & Houchmandzadeh, B. (1994). Buckling of a bidimensional solid. Europhysics Letters (EPL), 28(8), 565–571. https://doi.org/ 10.1209/0295-5075/28/8/005.
- Schultz, D. G., Lin, X.-M., Li, D., Gebhardt, J., Meron, M., Viccaro, J., & Lin, B. (2006). Structure, wrinkling, and reversibility of langmuir monolayers of gold nanoparticles. *The Journal of Physical Chemistry B*, 110(48), 24522–24529. https://doi.org/10.1021/jp063820s.
- Silverberg, G. J., & Vecitis, C. D. (2017). Wrinkling and periodic folding of graphene oxide monolayers by langmuir–blodgett compression. *Langmuir*, 33(38), 9880–9888. https://doi.org/10.1021/acs.langmuir.7b02289.
- Thomas, A. N., & Borden, M. A. (2017). Hydrostatic pressurization of lung surfactant microbubbles: Observation of a strain-rate dependent elasticity. *Langmuir*, 33(47), 13699–13707. https://doi.org/10.1021/acs.langmuir.7b03307.
- Tordesillas, A., Lin, Q., Zhang, J., Behringer, R. P., & Shi, J. (2011). Structural stability and jamming of self-organized cluster conformations in dense granular materials. *Journal of the Mechanics and Physics of Solids*, 59(2), 265–296. https://doi.org/10.1016/j.jmps. 2010.10.007.
- Tordesillas, A., Pucilowski, S., Lin, Q., Peters, J. F., & Behringer, R. P. (2016). Granular vortices: Identification, characterization and conditions for the localization of

- deformation. *Journal of the Mechanics and Physics of Solids*, 90, 215–241. https://doi.org/10.1016/j.jmps.2016.02.032.
- Vargaftik, N. B., Volkov, B. N., & Voljak, L. D. (1983). International tables of the surface tension of water. *Journal of Physical and Chemical Reference Data*, 12(3), 817–820. https://doi.org/10.1063/1.555688.
- Waring, A. J., Walther, F. J., Gordon, L. M., Hernandez-Juviel, J. M., Hong, T., Sherman, M. A., ... Zasadzinski, J. A. (2005). The role of charged amphipathic helices in the structure and function of surfactant protein B. *The Journal of Peptide Research: Official Journal of the American Peptide Society*, 66(6), 364–374. https://doi.org/10.1111/j.1399-3011.2005.00300.x.
- Witten, T. A., Wang, J., Pocivavsek, L., & Lee, K. Y. C. (2010). Wilhelmy plate artifacts in elastic monolayers. *The Journal of Chemical Physics*, 132(4), 046102. https://doi.org/10.1063/1.3298997.
- Ybert, C., Lu, W., Möller, G., & Knobler, C. M. (2002a). Collapse of a monolayer by three mechanisms. The Journal of Physical Chemistry B, 106(8), 2004–2008. https://doi.org/10. 1021/jp013173z.
- Ybert, C., Lu, W., Möller, G., & Knobler, C. M. (2002b). Kinetics of phase transitions in monolayers: Collapse. *Journal of Physics: Condensed Matter*, 14(19), 4753–4762. https://doi.org/10.1088/0953-8984/14/19/301.
- Zasadzinski, J. A., Ding, J., Warriner, H. E., Bringezu, F., & Waring, A. J. (2001). The physics and physiology of lung surfactants. *Current Opinion in Colloid & Interface Science*, 6(5), 506–513. https://doi.org/10.1016/S1359-0294(01)00124-8.
- Zhang, H., Fan, Q., Wang, Y. E., Neal, C. R., & Zuo, Y. Y. (2011). Comparative study of clinical pulmonary surfactants using atomic force microscopy. *Biochimica et Biophysica Acta* (BBA)—Biomembranes, 1808(7), 1832–1842. https://doi.org/10.1016/j.bbamem.2011. 03.006.